



HAL
open science

Damage control of the masonry infills in RC frames under cyclic loads: a full-scale test study and numerical analyses

Qiwang Su, Gaochuang Cai, Meree Hani, Amir Si Larbi, Konstantinos Daniel Tsavdaridis

► To cite this version:

Qiwang Su, Gaochuang Cai, Meree Hani, Amir Si Larbi, Konstantinos Daniel Tsavdaridis. Damage control of the masonry infills in RC frames under cyclic loads: a full-scale test study and numerical analyses. *Bulletin of Earthquake Engineering*, 2022, 21 (2), pp.1017-1045. 10.1007/s10518-022-01565-y . hal-04092564

HAL Id: hal-04092564

<https://hal.science/hal-04092564v1>

Submitted on 28 Jan 2025

HAL is a multi-disciplinary open access archive for the deposit and dissemination of scientific research documents, whether they are published or not. The documents may come from teaching and research institutions in France or abroad, or from public or private research centers.

L'archive ouverte pluridisciplinaire **HAL**, est destinée au dépôt et à la diffusion de documents scientifiques de niveau recherche, publiés ou non, émanant des établissements d'enseignement et de recherche français ou étrangers, des laboratoires publics ou privés.



City Research Online

City, University of London Institutional Repository

Citation: Su, Q., Cai, G., Hani, M., Si Larbi, A. & Tsavdaridis, K. D. (2022). Damage control of the masonry infills in RC frames under cyclic loads: a full-scale test study and numerical analyses. *Bulletin of Earthquake Engineering*, 21(2), pp. 1017-1045. doi: 10.1007/s10518-022-01565-y

This is the accepted version of the paper.

This version of the publication may differ from the final published version.

Permanent repository link: <https://openaccess.city.ac.uk/id/eprint/29414/>

Link to published version: <https://doi.org/10.1007/s10518-022-01565-y>

Copyright: City Research Online aims to make research outputs of City, University of London available to a wider audience. Copyright and Moral Rights remain with the author(s) and/or copyright holders. URLs from City Research Online may be freely distributed and linked to.

Reuse: Copies of full items can be used for personal research or study, educational, or not-for-profit purposes without prior permission or charge. Provided that the authors, title and full bibliographic details are credited, a hyperlink and/or URL is given for the original metadata page and the content is not changed in any way.

City Research Online:

<http://openaccess.city.ac.uk/>

publications@city.ac.uk

1 **Damage control of the masonry infills in RC frames** 2 **under cyclic loads: A full-scale test study and numerical** 3 **analyses**

4 Qiwan SU¹, Gaochuang CAI^{2,3*}, Meree HANI⁴, Amir SI LARBI^{2,3},
5 Konstantinos Daniel Tsavdaridis ^{2,5}

6 1. Department of Civil Engineering, Southwest Jiaotong University, Chengdu, Sichuan,
7 China

8 2. International Research Organization for Advanced Science and Technology (IROAST),
9 Kumamoto University, Kumamoto, Japan.

10 3. Univ Lyon, Ecole Nationale d'Ingénieurs de Saint-Etienne (ENISE), Laboratoire de
11 Tribologie et de Dynamique des Systèmes (LTDS), UMR 5513, 58 Rue Jean Parot, 42023
12 Saint-Etienne Cedex 2, France

13 4. State Key Laboratory of Geohazard Prevention and Geoenvironment Protection,
14 Chengdu University of Technology, Chengdu, Sichuan, China

15 5. Department of Civil Engineering, School of Mathematics, Computer Science and
16 Engineering, City, University of London, Northampton Square, EC1V 0HB, London, UK

17 **Abstract**

18 This study investigates the effect of damage control methods on the seismic performance of
19 masonry infilled walls in reinforced concrete (RC) frames, by experimentally investigating
20 three full-scale infilled RC frames with different treatment details and finite element method
21 (FEM) analysis. The control methods included full-length connecting steel rebars, styrene
22 butadiene styrene (SBS) sliding layers, and two gaps between the wall and frame columns.
23 The results indicated that the ductility, wall damage, and residual deformation of the frame
24 with gaps or SBS layers were significantly improved. However, the initial stiffness, energy
25 dissipation capacity, and lateral load-carrying capacity of the frames with SBS sliding layers
26 all were reduced. The fully infilled frames exhibited a better lateral load-carrying capacity,
27 stiffness, and energy dissipation capacity, but presented larger lateral residual deformation
28 and lower ductility. The damage of the infilled walls in RC frames can be controlled by using
29 longer connecting rebars. The gaps and sliding layers can both significantly reduce the in-
30 plane damage of the walls. A simplified FEM model was proposed and applied to conduct a
31 parametric analysis for an in-depth study of fully infilled RC frames with and without sliding
32 layers. The results show that SBS is the optimal sliding layer material, and its optimal spacing
33 in RC frames is recommended as 1000mm.

34 *Keywords:* Damage control; Masonry hollow bricks, sliding layers; Wall collapse ratio; FEM

35 1 Introduction

36 Most of the infill in existing reinforced concrete (RC) frame structures in the world are
37 still made of unreinforced brick/block masonry. There is usually an interaction between non-
38 structural infill panels and the primary structural frame elements under an earthquake. The
39 influence of infills may positively or negatively affect the seismic vulnerability of the RC
40 frames, depending on the properties of masonry and the regularity of their disposition [1-2].
41 In China the load-carrying of infilled walls is usually ignored in the design of RC frame
42 structures for they are used just to divide the space, however, their weight is added to the
43 frames as a fixed force. In this case, more and more lightweight infilled walls are used in
44 filled RC frames, such as masonry hollow brick (MHB). On the other hand, MHBs can
45 minimize the adverse impact of the infilled walls on their surrounding frame beams and
46 columns. However, the walls are easy to be damaged under reversed lateral loads caused by
47 earthquakes for their low strength and large void ratio, which seriously affects the use of
48 residents and causes huge economic and social losses. This fact means that infill wall damage
49 during earthquakes needs to be controlled [3-5].

50 Up to now, many treatment methods have been proposed for controlling the damage of
51 infilled walls under earthquakes. They can be mainly divided into two types, (1)
52 strengthening or improving structural materials such as using shock-absorbing mortars and
53 steel fiber mortars, and (2) structural measures for infills such as reinforcing the infills [6-7],
54 adding damping or energy dissipation devices, and separating infills from the frame beams
55 and columns [8]. Wang and Ye [9-10] suggested using rubber concrete and foamed concrete
56 blocks to improve the seismic behavior of RC frames respectively and studied their seismic
57 performance experimentally and numerically. Moghadam et al. [11] proposed to use RC
58 panels to reinforce infilled walls in RC frames and studied their horizontal reinforcement and
59 bond beams effect through experiments. Sahota and Riddington [12] proposed to install a
60 lead layer between infilled wall and frame beams based on the theory of frame column creep
61 shortening. Mohammadi and Akramir [13] analyzed the seismic performance of RC frames
62 after removing their infilled wall corners and partially weakening RC frame columns. Their
63 results showed the developed system acted as a sacrificial element just like a fuse to protect
64 the infilled walls and frame elements. Yang and Ou et al. [14] commented that the damage
65 of the infill wall frames with energy dissipating devices wall was reduced. Zhou et al. [15]
66 reported that the seismic performance of RC frames with viscous dampers and styrene-
67 butadiene-styrene thermoplastic elastomer (SBS) and the damage control of their walls were
68 improved significantly. Perera et al. [16] proposed an infill panel with K-bracing containing
69 a vertical shear link. With this approach, the stiffening effect provided by the masonry was
70 kept while the low ductility of the frames was compensated with the energy dissipation action
71 of used link elements.

72 In addition, additional reinforcing layers on the surface of infilled walls also were
73 considered could to control the damage of the walls. Sevil et al. [17] proposed using steel
74 fiber reinforced mortar (SFRM) to reinforce hollow brick infill walls into strong and rigid
75 infills. Its ease of construction makes SFRM layer a frequently used damage control
76 technique for the infilled walls of RC frames, despite the higher cost of fiber reinforced
77 materials [18-19]. Ferro-cement jacket reinforced with welded steel mesh [20], and Epoxy-

78 bonded fiber-reinforced polymer (FRP) laminates [21][22] also were proposed to enhance
79 the strength of masonry infilled walls. Preti et al. [23-25] proposed partitioning infill earthen
80 masonry walls by horizontal wooden planks that allow a relative sliding between the
81 partitions. The combination of the deformability of earthen masonry and the sliding
82 mechanism occurring along the wooden planks made the walls have a high ductility capacity
83 during their in-plane response, significantly reducing their stiffness and strength at the same
84 time compared with traditional solid infills.

85 Expect for the experimental studies mentioned above, many numerical studies were
86 conducted to study the seismic performance of RC frames with infilled walls. Bartolomeo et
87 al. [2] proposed an alternative plane macro-element approach for the seismic assessment of
88 infilled frames. The approach validation was focused on recent experimental and numerical
89 results that investigate the influence of non-structural infills. Caliò and Bartolomeo [26]
90 presented a macro-modeling approach for the seismic assessment of infilled frame structures,
91 and the interaction between the frames and infills was simulated. Prateek et al. [27] developed
92 a novel computational modeling strategy using ABAQUS to investigate the in-plane behavior
93 of RC frames with infilled walls and rubber joints. They also proposed a masonry hollow
94 brick to reduce damage to infilled RC frames and pointed out that the frames tended to a
95 stable load-displacement relation because most of the seismic energy was dissipated by the
96 relatively weak masonry infills. However, to improve the collapse resistance of MHB infills
97 in the RC frames at the large displacement stage, previous research [28] suggested several
98 measures such as sufficient connection rebars at the bottom of the frame beams and the ends
99 of the infilled walls (1/3 column height). Moreover, a lightweight concrete panel could be a
100 good potential infill to get a higher wall-collapse resistance in the MHB-filled RC frames
101 according to the full-scale tests conducted by the authors of the paper [29]. The MHB-filled
102 RC frames performed a reasonable and stable lateral resistance behavior and ultimate
103 capacity under an earthquake.

104 In summary, previous studies have mainly focused on strengthening infilled walls,
105 separating the filled wall from structural frames and adding dampers to reduce damage. These
106 measures improved the seismic performance of the filled walls under earthquakes to a certain
107 extent and reduced wall damage and collapse. However, the strengthening of infilled walls
108 may increase the additional adverse impact on the seismic performance of RC frame
109 structures. The idea of adding energy-consuming or damping devices comes from the concept
110 of structural earthquake resistance and effectively reduces wall damages by increasing the
111 damping of the filled walls. However, its structures and construction process are usually
112 complicated and expensive, which limits its widespread use. The separation of infills from
113 frame beams and columns is mainly to reduce the strut effect of infilled walls under reversed
114 loads caused by earthquakes, however, its waterproof and sound insulation performance is
115 considered to be slightly poor. As a hollow lightweight material, MHB has the potential to
116 be an ideal filling material for infilling walls in RC frames for its better sound insulation and
117 heat preservation. To reduce the damage of the MHB infilling walls in RC frames under
118 earthquake attack, a rigid connection for the structural measure of the MHB infilled walls
119 with sliding layers is introduced here to replace the traditional rigid connection of MHB walls
120 by using the ideal sliding failure modes of walls. The objectives of this paper were to
121 investigate experimentally and numerically the effect of MHBs infilled walls with sliding

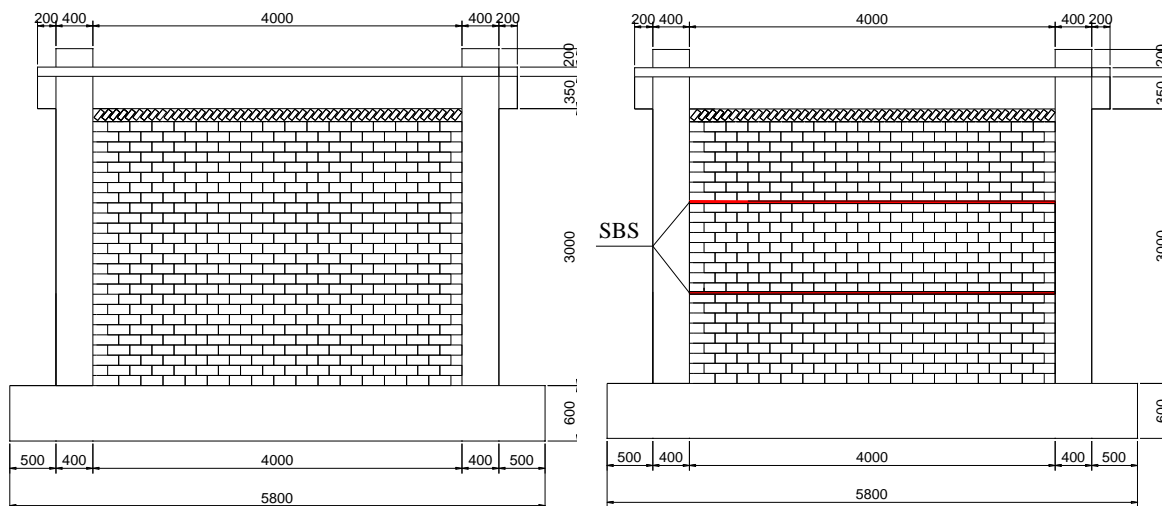
122 layers on the seismic behavior of infilled RC frames and comprehensively compare different
 123 damage control methods. Through a finite element analysis, a detailed discussion of
 124 experimental and numerical results of full-scale MHB-filled RC frames was presented, and
 125 a comparative study of control methods was provided.

126

127 2 Experimental program

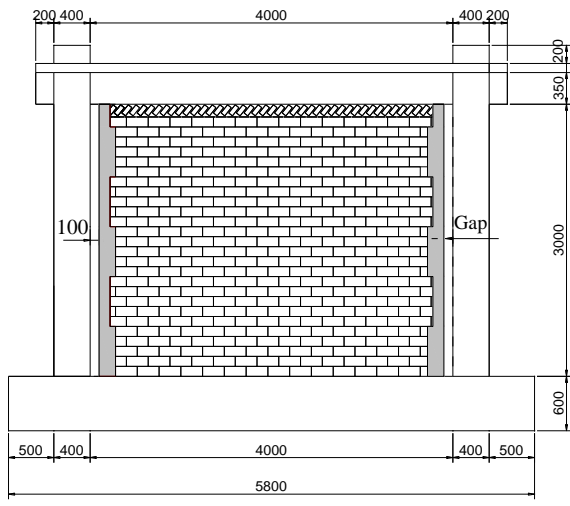
128 2.1 Test specimens

129 All tested specimens are full-scale one-bay-one-story MHB-filled RC frames designed as
 130 per Chinese design codes [30,31]. The details of dimensions and reinforcement of the frames
 131 are plotted in Figure 1. The sectional dimensions of the columns were 400 mm ×
 132 400mm ($b \times h$), while that of the beams was T-shape with the dimension of 200mm × 450mm
 133 × 1000mm × 100 mm ($b \times h \times b_f \times t_f$). The base beams used a larger section with a dimension of
 134 500mm × 600 mm ($b \times h$), as shown in Figure 1. Six 16 mm deformed bars, four 16 mm
 135 deformed bars, and six 16 mm deformed were used as the longitudinal reinforcements in the
 136 frame columns, frame beams, and base beams, respectively. The steel stirrups of the frame
 137 beam, columns, and base beam all were 8 mm diameter plain rebars with a spacing of 200.0
 138 mm and 135-degree hooks. The connection rebars were planted into the wall and connected
 139 with frame columns, as shown in Figure 1 (b) and (d). The aspect ratio of all walls, l_w/h_w (l_w
 140 and h_w are the length and height of the walls), was 1.33.

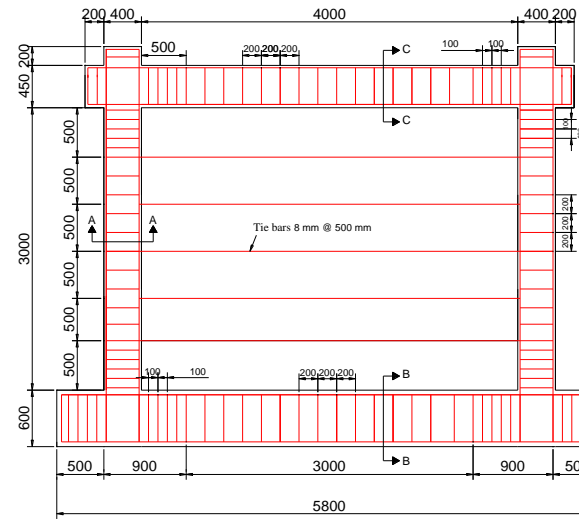


(a) Specimen 1 Full-infilled RC frame

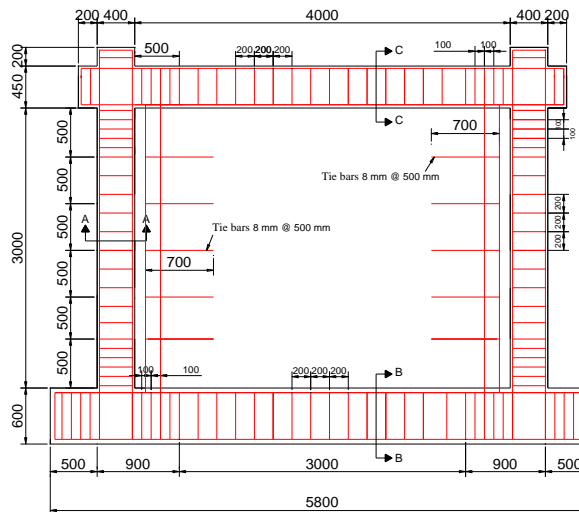
(b) Specimen 2 Full-infilled RC frame with SBS



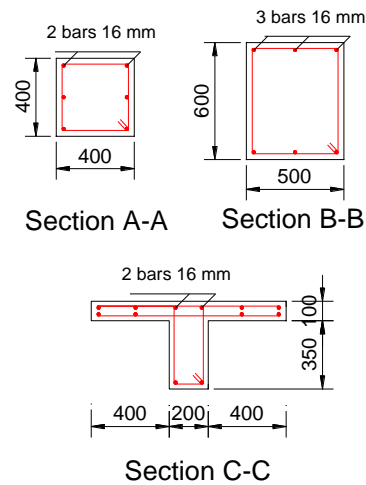
(c) Specimen 3 Full-infilled RC frame with gaps



(d) Reinforcement details of Specimens 1 and 2



(e) Reinforcement details of Specimen 3



(f) Details of columns and beams in all specimens

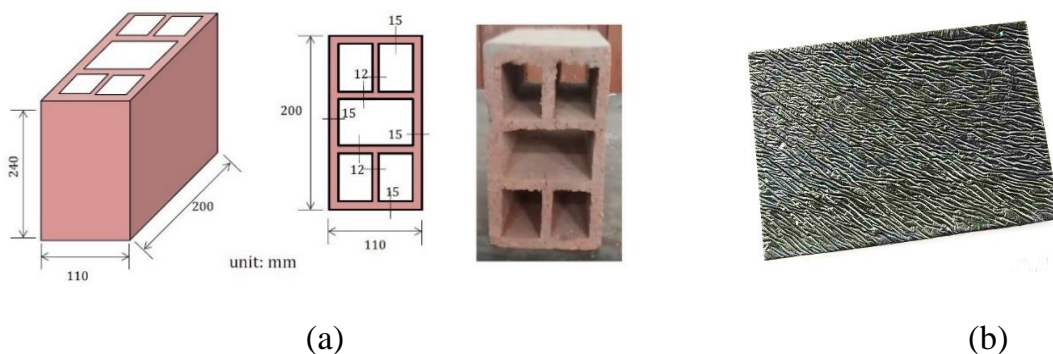
141

Figure 1 Dimensions and reinforcement of the tested frames

142 Specimens 1 and 2 were infilled fully with MHB walls connected with ten full-length
 143 horizontal connection rebars at five levels, which include two 8.0 mm diameter plain bars
 144 at each level with the same spacing and were fixed in the mortar layer between the bricks. In
 145 Specimen 2, two SBS slip layers were arranged inside the infilled wall with the same spacing
 146 from the wall bottom. The SBS layers were placed between the bricks without mortar.
 147 Specimen 3 applied ten horizontal connection bars, divided into 5 levels (spacing = 700.0
 148 mm), where each level had two plain bars (diameter = 8 mm) with the same spacing from the
 149 wall bottom. All rebars were fixed in the mortar layers between the bricks. Two full
 150 separation gaps were designed between the filled wall and the frame columns in the direction

151 of wall height, with a width of 100.0 mm, as shown in Figure 1 (c). In addition, to prevent
152 the wall from collapsing prematurely due to the two gaps during the test, two detailing
153 columns were constructed on both sides, which were staggered by MHBs and their
154 longitudinal reinforcements passed the holes of bricks filled by mortar.

155 All frame beams and columns were made of normal compressive strength concrete. The
156 average cube compressive strength of the used concrete (size $100 \times 100 \times 100 \text{ mm}^3$) was 33.5
157 N/mm^2 (prismatic concrete compressive strength, $150 \times 150 \times 300 \text{ mm}^3$, 14.3 N/mm^2), whose
158 elastic modulus was 30.0 kN/mm^2 obtained by standard tests [30,31]. For the longitudinal
159 and transverse reinforcements, the yield strength of the used 8mm and 16 mm diameter plain
160 rebars were 480 N/mm^2 and 420 N/mm^2 [32], respectively. The frames were infilled with
161 MHBs ($240 \text{ mm} \times 200 \text{ mm} \times 110 \text{ mm}$, see Figure 2), which are the same as the bricks in the
162 literature [28,29]. The ratio of net area to the gross area of the bricks was 47.85%, and the
163 average weight per unit of the bricks was about 4.96N. The thickness of mortar used for the
164 walls was between 7mm to 10mm. The average compressive and tensile strengths of the
165 mortar used in all frame specimens were 5.62 N/mm^2 and 0.45 N/mm^2 , respectively, through
166 standard tests [33]. The average compressive strength of the used masonry brick in the
167 direction of its holes was 3.5 N/mm^2 , considering the gross area of the bricks. The SBS layer
168 is made of polyester felt, glass fiber felt, and glass fiber reinforced polyester felt as the base,
169 and asphalt using a modifier of SBS. Its thickness and density were 3.0 mm and 34.3 N/m^2
170 respectively, and covered with polyethylene film as isolation materials, as shown in Figure
171 2. The dissoluble composite of the membrane of the SBS layers was 2100 g/m^2 and its
172 elongation at maximum tensile force can be over 35%. The maximum tensile force load along
173 the length direction of the layers (test specimen length 200 mm and width 50 mm) was
174 3.33 N/mm^2 .



175

176

177

178

179

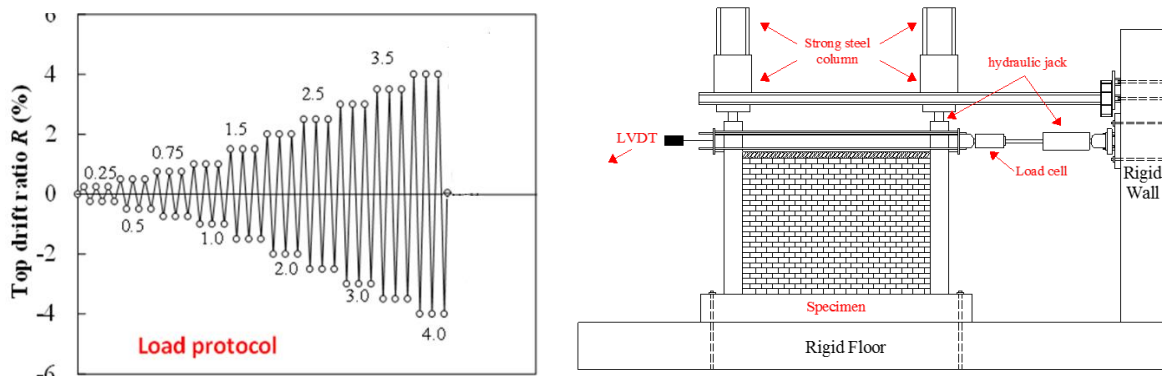
180 2.2 Test setup and load history

181

182

The details of the test setup and instrumentations are presented in Figure 3. The base beams of the specimens were fixed to a strong floor through several high-strength steel bolts.

183 Each specimen was tested under a combination load with reversed cyclic lateral load and a
 184 constant axial load. The lateral load was applied at the upper frame beams using a hydraulic
 185 jack shown in Figure 3, while the axial load was applied at the top of the columns by two
 186 hydraulic jacks. The applied axial load in each column was 572.0 kN, about 25% of the axial
 187 load capacity of the columns calculated based on concrete prismatic compressive strength.
 188 To confirm the possible move of the specimens during the tests, two linear variable
 189 differential transducers (LVDTs) were used at the ends of the base beams. One LVDT was
 190 applied at the load level to measure the lateral displacement of the specimens to calculate the
 191 drift ratio of the specimens (R) to control the lateral loading.



(a) Load history

(b) Test setup

Figure 3 Load protocol and test setup.

195 As shown in Figure 3, a reversed cyclic lateral load was conducted at the top frame beam
 196 of each specimen, after the designed axial load was applied on the top of the two frame
 197 columns. To observe the first crack of the infilled walls, the loading method at the beginning
 198 of the test is designed to be force-controlled until the drift rate was 0.25%, in both directions.
 199 Afterward, three full cycles of displacement-controlled loading were conducted at the
 200 subsequent target loading cycles until the drift ratio was 4.0%. The main test observations
 201 included cracking, damage, and collapse of the bricks, all of which were carefully recorded
 202 during the tests. The tests were ended when (1) the drift ratio reached 4.0 % to ensure the
 203 safety of researchers and test devices, or (2) the frame failed to resist the applied loads making
 204 the load-carrying capacity below 50% of the peak load.

3 Experimental results

3.1 General observations

207 As shown in Figures 4 to 6, the treatment methods in the walls present a significant
 208 influence on the seismic performance of infilled RC frames. For Specimen 1, when the drift
 209 ratio was 0.25%, several cracks were observed, including diagonal and horizontal cracks on
 210 both sides of the wall, transverse cracks in the middle of the frame columns, and the diagonal
 211 zone at the ends of the frame beam (upper beam, same as below). When R reached 0.5%,

212 new cracks appeared inside the frame columns and were roughly distributed on the infilled
 213 wall. The previous cracks at the ends of the beam extended to the beam edges and the beam-
 214 column joint zones. While R was 1.0%, several cracks were observed in the mortar in the
 215 middle of the wall and the zones of the connection rebars. Some connecting steel bars were
 216 exposed and the mortar layer is completely peeled off. The mortar on the wall's middle sides
 217 fell off and the upper connection bars were slightly bent outside when R reached 1.5%, and
 218 several bricks were crushed and fell off on both sides of the wall at the same time. When R
 219 was 2.0%, the cracks in the columns developed significantly, while the connecting rebars
 220 were bent seriously and the bricks continually fell off from $R=2.5\%$. After R exceeded 3.0%,
 221 the wall top was separated from the upper beam bottom, and more connecting bars were
 222 exposed. Before $R=3.50\%$, the wall subsidence occurred in the specimen middle, and more
 223 bricks were crushed and more connecting rebars were seriously bent. At $R=4.00\%$, the
 224 infilled wall collapsed almost completely, as shown in Figure 4 (a), making the wall exhibit
 225 a similar structural behavior to a bare RC frame.



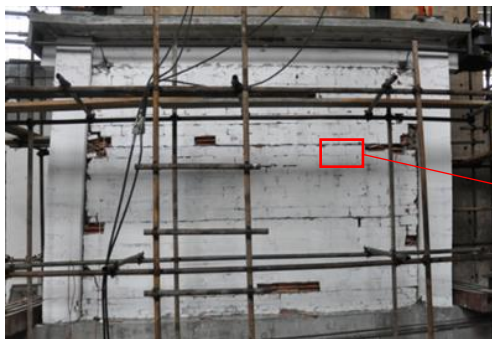
(a) front view of wall collapse



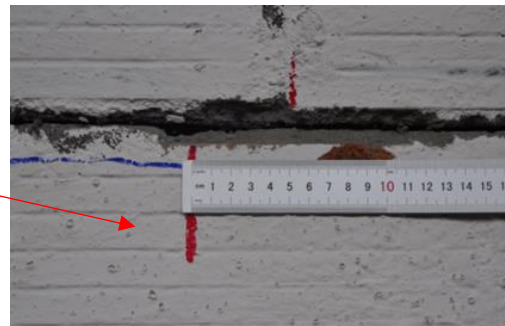
(b) back view of wall collapse

226

Figure 4 Damage of Specimen 1 at $R=4.0\%$



(a) overall damage at $R=4\%$



(b) slippage of SBS layer at $R=2\%$

227

Figure 5 Overall damage of Specimen 2 and slippage of the SBS layers

228 Regarding Specimen 2, as shown in Figure 5 (a), the use of SBS layers significantly
 229 reduced the damage and collapse of the infilled wall. At $R=0.25\%$, several cracks were
 230 observed along the SBS layers, at the bottom corner of the wall, the middle and bottom of

231 the columns, and the end of the frame beam. When R reached 0.50%, the wall was divided
232 into three parts by the two SBS layers, and the previous cracks were developed slowly until
233 R=1.0%. From R=1.25%, the SBS layers started to slide freely in the wall. In general, the
234 cracks and damage to the wall were much smaller than those of Specimen 1. Major cracks
235 and damage were concentrated on the two bottom edges of the wall. The corner bricks and
236 beam bottom concrete were crushed and the internal longitudinal reinforcements were
237 exposed in the beam. After R=1.75%, several cracks appeared on the columns and the wall
238 sides. When R=2.00%, only the bricks at the corners of the three small walls were crushed.
239 This means that the diagonal resistance struts were formed in each small wall. However,
240 due to slippage of the SBS layer, the diagonal strut was weak and insufficient to form
241 diagonal cracking damage. The three small walls separated by the layers continued to slide
242 along the layers. As shown in Figure 5 (b), the slip displacement reached 50.0mm at R=2.0%.
243 After R exceeded 3.0%, the three small walls continued to slide, as well as the bricks were
244 crushed, fell off, and expanded horizontally until the end of the test. The cracks extended at
245 the beam ends and the bottom of the columns, but the wall was intact with less damage
246 compared with Specimen 1.

247 For Specimens 3, several diagonal cracks occurred in the wall and developed rapidly
248 at the beginning. When R reached 0.50%, the bricks at the top of the wall fell off and some
249 cracks were observed between the wall and the columns, at the frame beam ends. When the
250 drift ratio reached 0.75%, more bricks fell off and were crushed at the inside edge of the
251 columns, and the previous cracks were developed quickly. The beam-column joint zones
252 were damaged and local concrete fell off at the same time. When R exceeded 1.0%, all cracks
253 observed previously were developed further and new cracks appeared in the middle of the
254 columns. The collapsed area of the wall was increased and concentrated near the ends of the
255 columns, but the collapse ratio was still small until R=1.25%. At R=1.50%, the large increase
256 in the cracks and collapsing in the middle of the wall was not obvious because the wall was
257 separated from the detailing columns. From that moment on, the frame behaved as a bare RC
258 frame. When R=1.75%, the wall was damaged slightly, the concrete at the beam bottom was
259 crushed, and the steel rebars of the columns were buckled slightly. After that, the rebars of
260 the columns were severely buckled and the concrete at the beam ends was crushed heavily
261 as well. As R reached 2.50%, several steel rebars of the columns were broken, while the
262 rebars of the frame beam were severely buckled. The infilled wall was in close contact with
263 the frame columns on both sides at R=3.0%, and the longitudinal steel rebars at the beam
264 ends were fractured, leading to the final failure of the frame at R=4.0%. In summary, all
265 described cracks and damages were distributed in the infilled wall and several bricks fell off
266 from the frame, however, the wall was intact and the frame was protected well, as shown in
267 Figure 6.



268

269

Figure 6 Damage of Specimen 3 at R = 4%

270 3.2 Hysteretic behavior and skeleton curves

271 The lateral load-displacement hysteretic curves of all specimens and their skeleton
272 curves are presented in Figure 7, which both are important to assess the seismic behaviors of
273 the specimens. The results show the load-carrying capacity of the specimens is greater than
274 that of the bare frame made with the same bricks in the previous study [28]. Due to the
275 influence of the infills, the skeleton curves of Specimens 1 and 3 present distinct peaks (See
276 Figures 7 (a), (c), (d)). After adding the SBS layers to Specimen 2, the strut effect of the
277 infilled wall was significantly weakened and the skeleton curve did not present an obvious
278 peak (see Figure 7 (b)). As shown in Figure 7 (c), the hysteretic curve of Specimens 3 was
279 firstly a vertical long-narrow shape but rapidly changed to a long-fat shape. Besides, the
280 curve appeared a sudden increase in load-carrying capacity when R reached 2.5%. The
281 closing of the gaps on both sides of the wall was the main reason for the increase in the
282 capacity. The skeleton curves plotted in Figure 7 (d) show that the skeleton curve of
283 Specimen 1 increases to its maximum capacity at R=0.50% and then decreases sharply until
284 about 2.0%, followed by a short stable stage until R=3.0%. Besides, compared with
285 Specimen 1, the curve of Specimen 2 was more stable in increasing and decreasing phases in
286 both directions. However, both the maximum load-carrying capacity and initial stiffness were
287 smaller than those of Specimens 1 and 3, especially its maximum capacity was only 3/4 times
288 that of Specimen 1. For Specimen 3, the curve reached the first peak load at R=0.50%, then
289 slowly declined with a similar downward trend to that of Specimen 1 and ended at R=2.0%.
290 After that, the load-displacement curve increased to its second peak load when R reached
291 3.0% to 4.0%, which was larger than the first peak load. As the lateral displacement increased,
292 the lateral load dropped sharply to a similar level to those of the other two specimens. With
293 the lateral load increasing, the bending and damage of the detailing columns increase
294 continuously, and its load-carrying capacity decreases gradually. As the detail columns bent
295 causing the gaps between the wall and detailing columns to be closed, the bearing capacity
296 increased gradually. After that, the bearing capacity decreased again and a second peak
297 occurred as the wall damage intensifies. It was understood that Specimen 3 reached its
298 ultimate load (the first peak) at R = 0.5%, however, the specimen provided a higher load-

299 carrying capacity because the detailing columns made the wall contact with the frame
 300 columns, further increasing the ultimate capacity of the specimen. Compared with Specimen
 301 1, Specimen 3 provided a small early peak capacity because the gaps between the frame and
 302 infilled wall reduced the diagonal strut effectiveness of the infills. But after the gaps were
 303 closed at the corners, Specimen 3 could provide almost the same level of capacity as
 304 Specimen 1 at the same displacement.

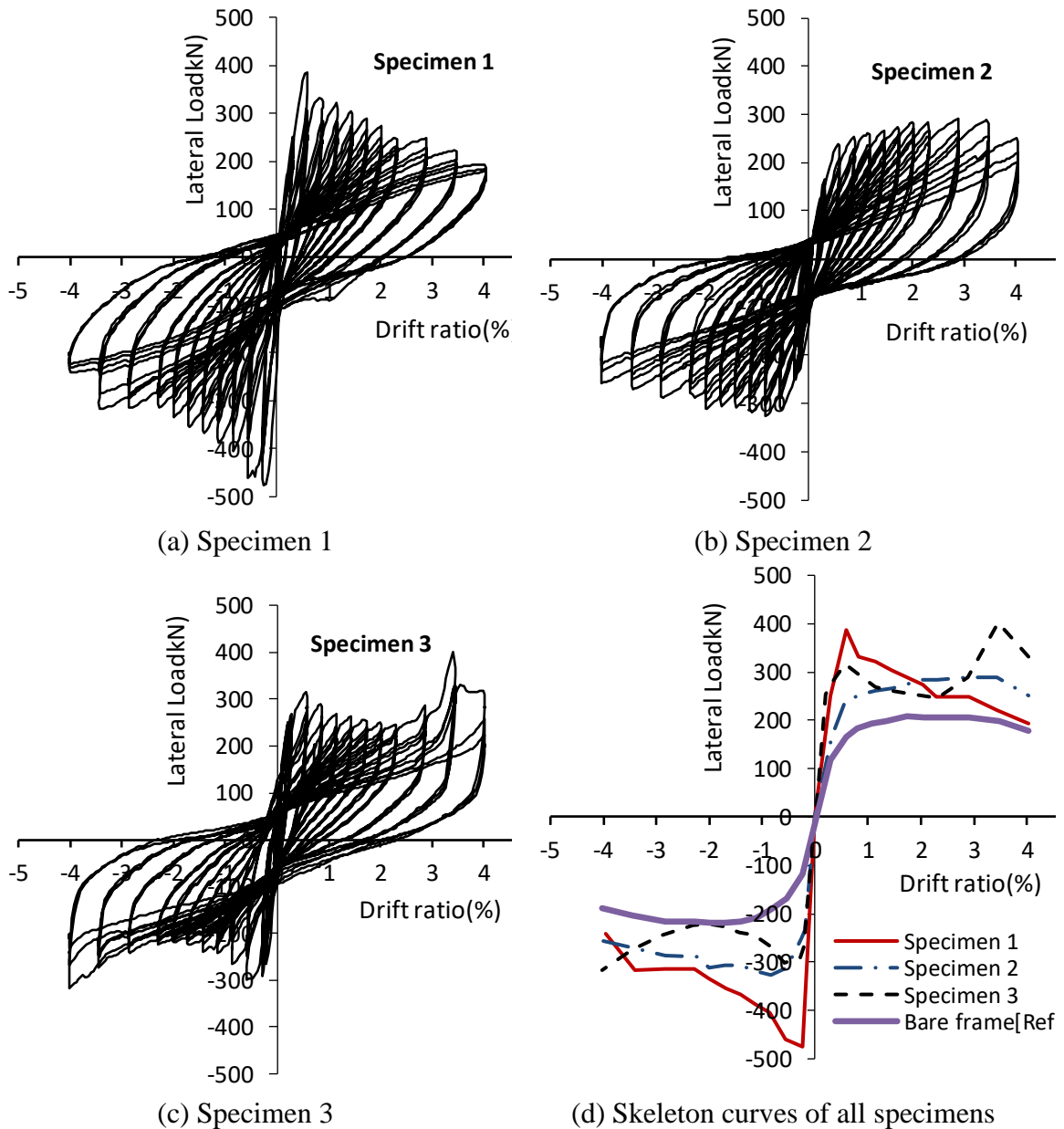


Figure 7 Lateral load-displacement curves of tested specimens

305

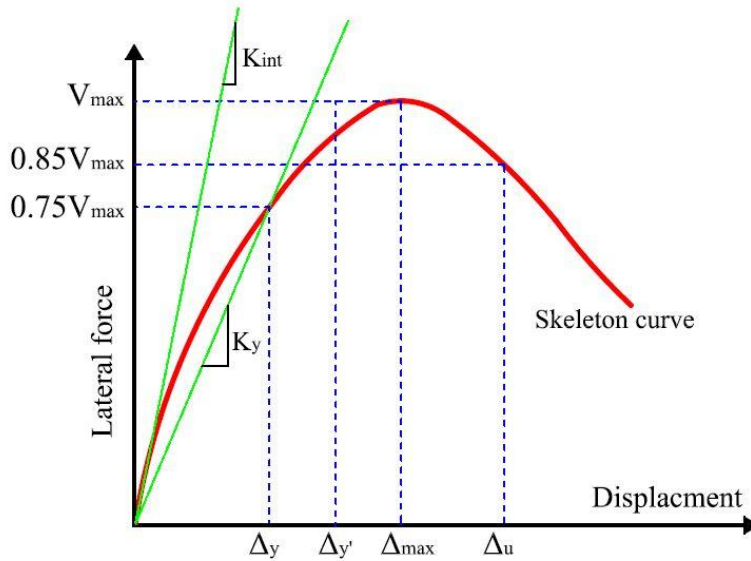
3.3 Ductility, stiffness, and energy dissipation

3.3.1 Initial stiffness and ductility

The initial stiffnesses discussed in this study include mainly initial elastic deformation stiffness K_{int} and yielding stiffness K_y , as shown in Figure 8. The stiffnesses were calculated as secant displacement stiffness corresponding to 0.33 and 1.0 times the measured yielding displacement (Δ_y) of the specimens, respectively. The yielding displacement was the measured displacement corresponding to (1) the yielding point of the skeleton curves of the load-displacement curves of the elements or (2) when certain longitudinal rebar in the frame columns reached its yield strength. In the present study, taking the yielding displacement Δ_y of the infilled frames as the measured displacement corresponding to $0.75V_{max}$, and using maximum lateral displacement (Δ_{max}) and ultimate displacement (Δ_u) corresponding to $85\% V_{max}$ [34,35], the maximum and ultimate ductility of the frames (μ_{max} and μ_u) are calculated as Eq. (1). The ultimate drift ratio δ_u was calculated using the ultimate displacement divided by specimen height (H), which is calculated as Eq. (2).

$$\mu_{max} = \frac{\Delta_{max}}{\Delta_y}, \quad \mu_u = \frac{\Delta_u}{\Delta_y}, \quad \Delta_y = \frac{4}{3} \Delta_y \quad (1)$$

$$\delta_u = \frac{\Delta_u}{H} \times 100 \quad (2)$$



321

322

Figure 8 Definition of ductility and stiffness on the skeleton curves

323

324

325

326

Table 1 lists the main experimental results of all specimens. Compared with Specimen 1, the other specimens presented a higher ductility. In Specimen 2, the sliding layers reduced the damage of the infilled wall because the layers separated the wall into three small walls with diagonal struts avoiding the damage of the central wall at the post-peak stage. This also

327 resulted in mitigation in the degradation of the load-carrying capacity at the stage. However,
 328 due to the low elastic property of the SBS layers, the initial stiffness of Specimen 2 was
 329 smaller than that of the other specimens. The high ductility of Specimen 3 was because the
 330 gaps released the deformation of the wall. The specimen also exhibited the highest initial
 331 stiffness as the detailing columns made the frame have larger structural integrity at the initial
 332 stage.

333 **Table 1 Summary of results of test specimens**

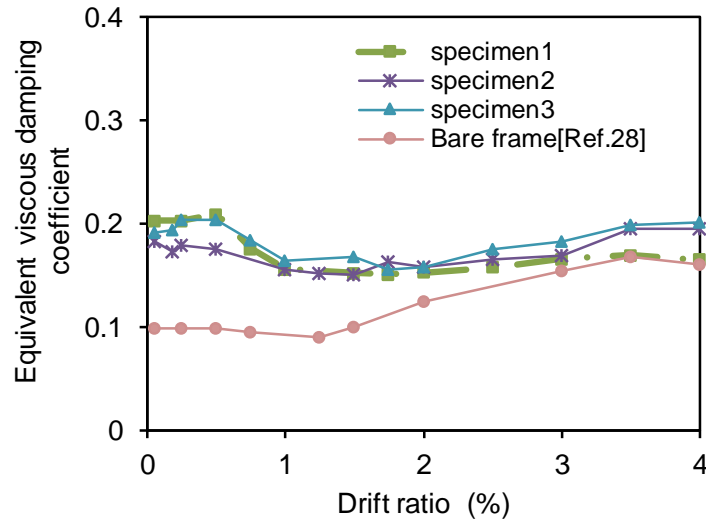
Specimens	V_{\max}^a (kN)	V_{\max}^b (kN)	K_{int} (kN/mm)	K_y (kN/mm)	Δ_y (mm)	Δ_{\max} (mm)	Δ_u (mm)	μ_{\max}	μ_u	δ_u (%)
1	387.34	476.18	26	22.06	12.55	19.57	48.98	1.17	2.93	1.52
2	290.14	327.02	16.39	12.13	16.24	95.58	135.50	4.41	6.26	4.20
3	403	317	35.52	9.89	16.14	114.06	130.32	5.30	6.06	4.04

334 (a) Push direction, and (b) Pull direction

335

336 3.3.2 Energy dissipation capacity

337 The equivalent viscous damping coefficient (h_{eq}) defined by previous research [36] was
 338 applied in this study to discuss the energy dissipation capacity of the specimens. Figure 9
 339 presents the development of the h_{eq} coefficient-drift ratio curve of all specimens. The results
 340 indicate that the infill properties, gaps, and the sliding layer all have a significant influence
 341 on the energy dissipation capacity of the frames, especially at the early stage of loading.
 342 Because the sliding layer reduced the diagonal strut action of the infills, the self-restoring
 343 capacity of the infilled RC frame was increased resulting in a significant decrease in the
 344 energy dissipation of Specimen 2. Besides, the additional gaps near the frame columns only
 345 influenced the energy dissipation capacity of the frame at the large deformation stage, as
 346 shown in Figure 9. Compared with the bare RC frame in the literature [28], an obvious
 347 decrease in the factor h_{eq} was observed in Specimen 1, in particular before the drift ratio
 348 reached 2.0%. The additional SBS layers made the energy dissipation capacity of the RC
 349 frame (No.2) higher than that of the bare RC frame [28] before R=3.0%, but a similar energy
 350 dissipation capacity was presented at the subsequent loading cycles.



351

352

Figure 9 Equivalent viscous damping coefficients versus drift ratios

353

3.3.3 Lateral residual deformation

354

355

356

357

358

359

360

361

362

363

364

365

366

367

368

369

370

371

The lateral residual deformation of structural elements represents their self-resilience capacity affecting the repair and strengthening of whole structures. In general, a RC frame is expected to recover for an easy repair after an earthquake, but the damage and plastic deformation accumulated on infilled walls during reverse lateral loads usually prevent RC frames from recovering. In this study, the residual drift ratio (R_{res}) of columns was the drift ratio corresponding to the lateral load equaling zero at the first loading loop with each target drift ratio. The calculated ratios were taken as the mean values obtained in both load directions in the study, which are presented in Figure 10. The results show that the residual drift ratios of all specimens increase stably with the target drift ratios. Specimen 1 presents the highest residual deformation as the wall was damaged significantly caused by the development of cracks and the strongest diagonal strut effectiveness in the fully infilled frame. While both Specimens 2 and 3 show almost the same behavior which means both the SBS layers and the gaps at both sides of the wall reduced the diagonal strut effect of the infills on the surrounding frame columns. This significantly increased the restoring of the frame columns and beams, which is similar to a bare frame, especially at the large deformation stage. The difference in the residual deformation caused by the different lengths of connecting rebars just can be observed before $R=2.0\%$, which may be attributed to the anchorage of the connecting rebars failing at the large deformation stage.

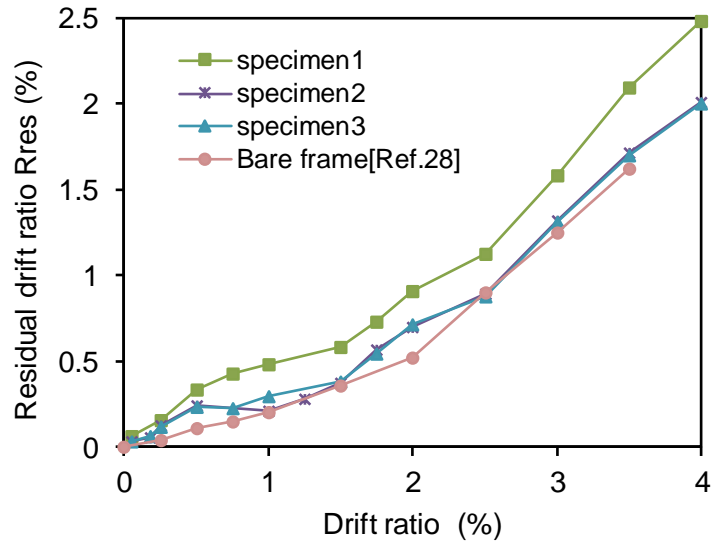
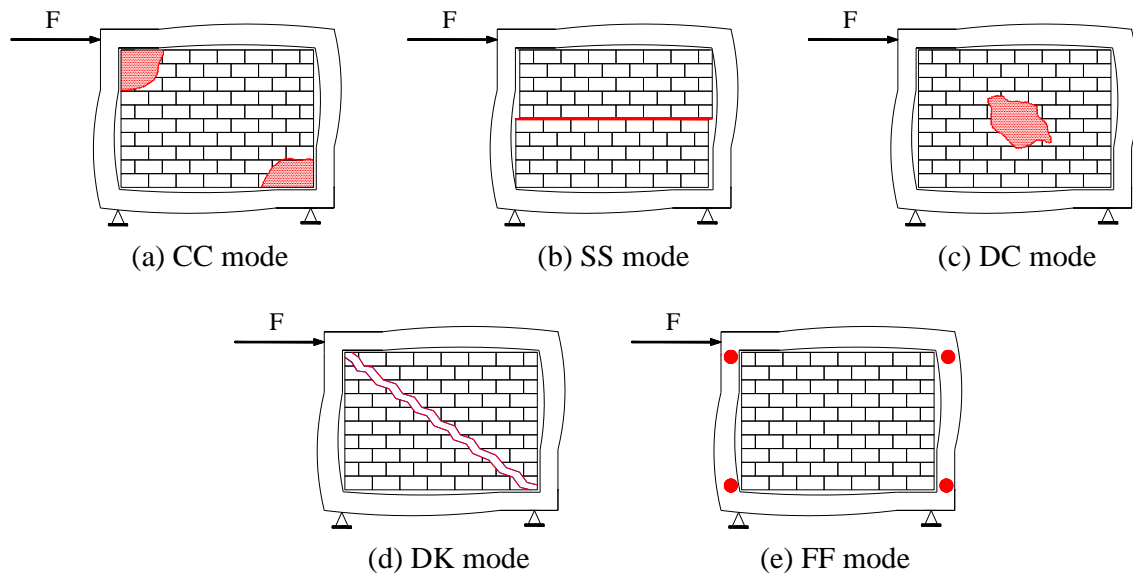


Figure 10 Evolution of residual deformation of the frames

3.4 Failure modes of infilled RC frames

The failure modes of the infill walls used the masonry bricks mainly include corner crushing failure (CC), sliding shear failure (SS), diagonal compression failure (DC), diagonal cracking failure (DK), and frame failure (FF), as same as previous research summarized in Figure 11[37]. Based on the experimental results, the failure modes of Specimens 1 to 3 are CC, SS, and CC modes, respectively.

The CC and DC failure modes are prone to occur in relatively strong RC frames with weak infill walls or RC frames with large aspect ratios. The MHBs or other lightweight blocks are used increasingly recently due to their suitable strength, which can produce the suitable diagonal strut effect of the infill wall in RC frames at the early stage of deformation. The CC and DC are the most common failure modes of infilled walls in China. When thin flexible layers are arranged in the horizontal brick joints of the hollow brick infill wall such as the SBS layer used in the study, the SS failure mode usually occurs in RC frames. Besides, the DK mode usually occurs when the frames or beam-column joints are relatively weak with a quite strong infill. It is worth mentioning that only CC and SS failure modes are of practical importance [38], while the DK mode occurs very rarely because solid bricks with high strength are no longer used in infilled walls in many countries such as China. Generally, the frames with DK failure modes can absorb more earthquake energy, however, their damage is much more serious than other frames. On the contrary, the damage of infilled walls in RC frames with FF failure mode is much smaller, but the frame joints are usually damaged seriously. It can be seen that the walls with SS, DC, and CC failure modes can effectively protect structural frames at the cost of serious damage to the infilled walls (except SS mode). This highlights the superiority of the treatment method in Specimen 2 with SS failure mode.



397

398

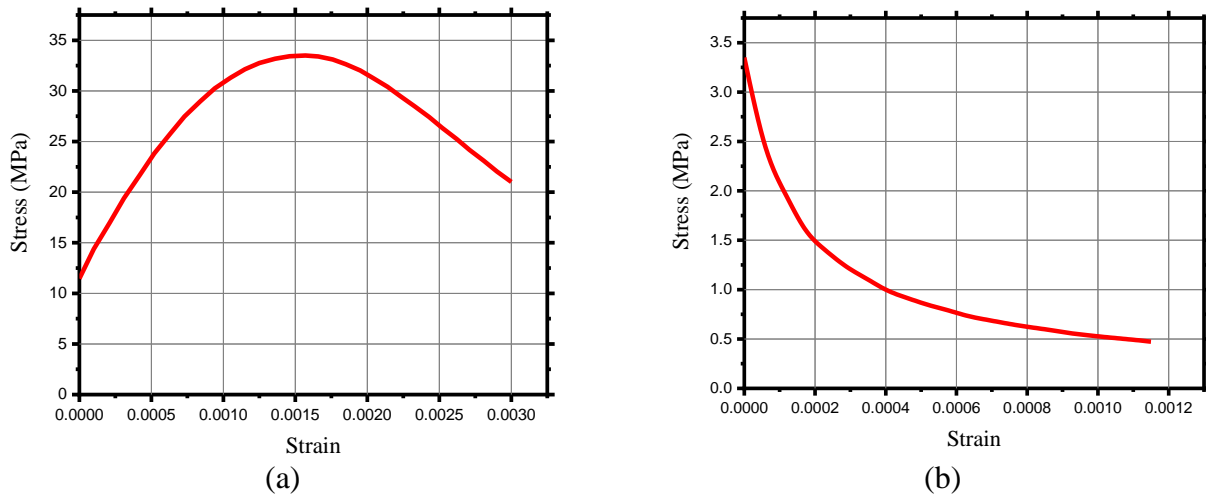
Figure 11 Different failure modes of masonry-infilled frames

399 4 FEM simulation

400 4.1 Modeling strategy

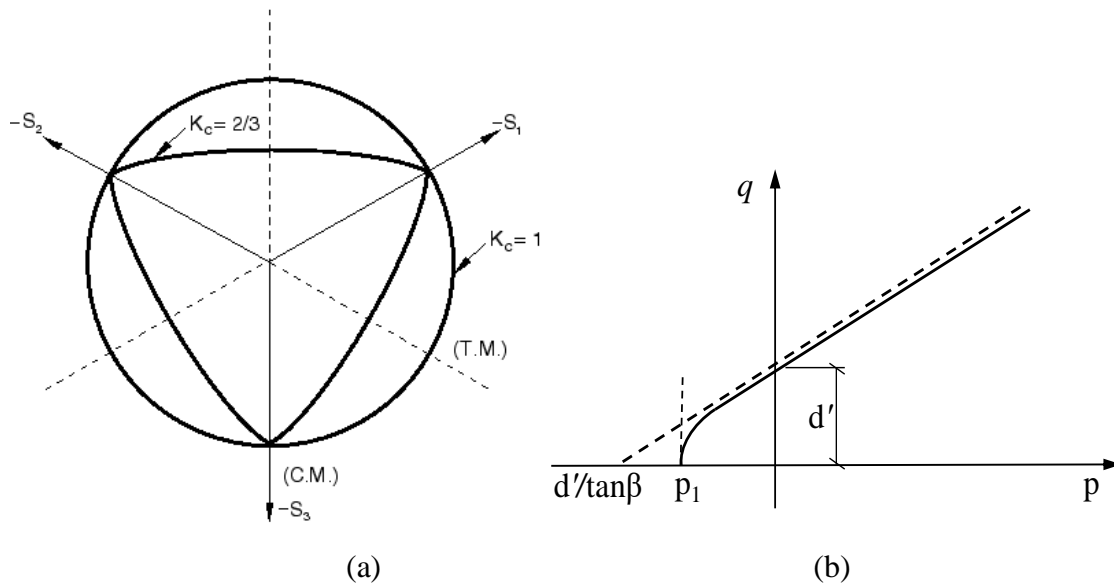
401 A commercial finite element method (FEM) analysis software *ABAQUS* was used to
 402 model the masonry infilled frames. Because the infilled wall was isolated from Specimen 3,
 403 which meant that the specimen was considered to be a bare frame to a certain extent, it was
 404 not simulated in the study. Specimens 1 and 2 were applied for optimizing FEM models
 405 working as two controlling specimens for the discussion below.

406 The three-dimensional 8-node solid element, C3D8R, was used to model the concrete
 407 frames, masonry units, and sliding layer (i.e. SBS layer, Basalt fiber-reinforced polymer
 408 (BFRP) laminate, and steel plate). The beam element (B31) was applied to model the steel
 409 reinforcements in RC frames and connection rebars in the infills of RC frames, which
 410 presented with an elastic-plastic material response. The Concrete Damaged Plasticity (CDP)
 411 model was applied to identify the non-linear behavior of concrete, in which the main failure
 412 was assumed as compressive crushing and tensile cracking [39,40]. Figure 12 shows the
 413 constitutive model applied in the study for the concrete materials under tension and
 414 compression.



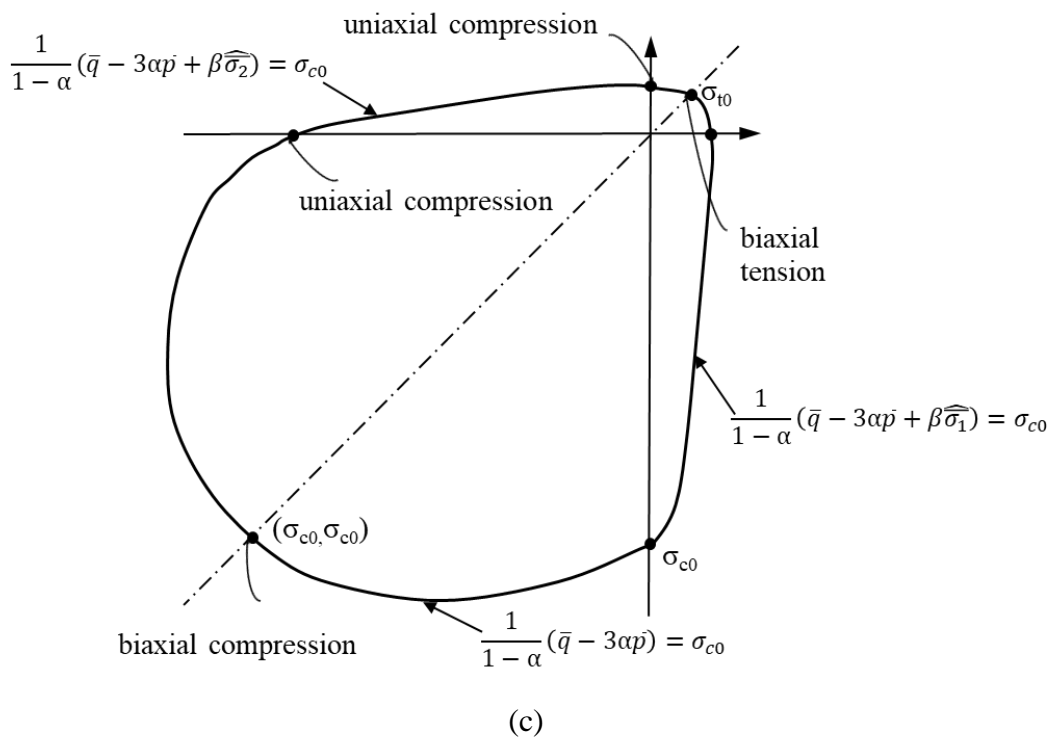
415 Figure 12 Constitutive models of concrete (a) under compression and (b) tension

416 Besides, the concrete model used a Drucker-Prager strength hypothesis modified by
 417 Lubliner [41], and Lee and Fenves [42]. For this, the failure surface in the deviatoric cross-
 418 section was determined by Parameter K_c . It is always greater than 0.5, and the deviatoric
 419 cross-section of the failure surface becomes a circle (as Drucker-Prager strength hypothesis)
 420 when K_c is 1.0. The study used the original CDP model recommend value assuming K_c as
 421 $2/3$ [43]. For this value, the shape is similar to the strength index (a combination of three
 422 mutually tangent ellipses) formulated by William and Warnke [44], which is a theoretical-
 423 experimental index based on tri-axial stress test results, as shown in Figure 13 (a). In addition,
 424 the plastic is adjusted by eccentricity (plastic potential eccentricity) in the CDP model, which
 425 was taken as 0.1 referring to the literature, which means the surface in the meridional plane
 426 becomes a straight line[39]. As shown in Figure 13 (b), the dilation angle in the CDP model
 427 was interpreted as a concrete internal friction angle, which was assumed as 36° according to
 428 the literature [39]. Besides, the viscosity parameter, μ , was ignored in Abaqus/Explicit
 429 analysis and was set as 0.0 [44]. Figure 13 (c) shows the constitutive behavior of the concrete
 430 materials under biaxial stress. Here, the ratio of the strength in the biaxial to the strength in
 431 the uniaxial σ_{b0}/σ_{c0} (f_{b0}/f_{c0}) was taken as 1.16 [44].



432

433



434

435

436

437

438

Figure 13 (a) Deviatoric cross-section of failure surface (b) hyperbolic surface of plastic potential in the meridional plane (c) constitutive model of concrete under biaxial stress

439

440

The masonry units were treated as continuum elements and modeled by the Drucker Prager plasticity model in ABAQUS, an inelastic constitutive model. In this study, a

441 compression hardening masonry continuum brick model was used, whose main material
 442 properties are listed in Table 2.

443 Table 2 Material properties for continuum bricks and mortar

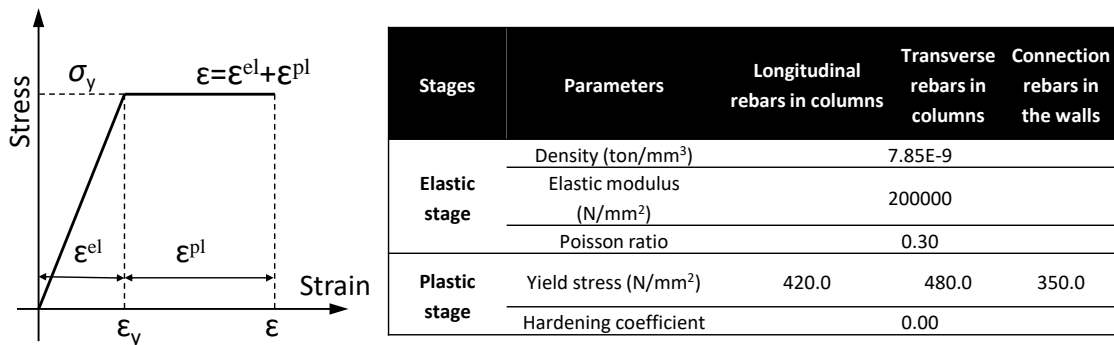
Properties	Parameters	Value
Elastic	Density (kN/m ³)	1900
	Modulus elasticity (N/mm ²)	20000
	Poisson ratio	0.15
Inelastic properties	Angle of friction	46°
	Flow stress ratio	0.8
	Dilatation angle	20°

444 The same SBS layer, BFRP laminate, and steel plate were used as the sliding layers
 445 in infilled masonry walls for comparative study, which all were considered elastic materials.
 446 The Young's modulus and Poisson's ratio as well as the coefficient of friction between bricks
 447 and the layers are listed in Table 3. Besides, the material properties of steel rebars are
 448 summarised in Figure 14. The total deformation, ϵ , is described as equal to the sum of elastic
 449 deformation (ϵ^{el}) and plastic deformation (ϵ^{pl}).

450 Table 3 Material properties of sliding layers

Parameters	SBS layer	BFRP laminate	Steel plate
Density (kN/m ³)	1240	2920	7850
Modulus elasticity (N/mm ²)	9.52	75000	200000
Poisson ratio	0.43	0.23	0.3
Coefficient of friction	0.32	0.75	0.64

451



452

453 Figure 14 Material model of steel materials

454 The coherent behavior methodology was used to determine the brick-to-brick and
 455 brick-to-frame interaction in this paper. The surface-based cohesive behavior provides a
 456 simplified way to model cohesive connections with negligibly small interface thicknesses,
 457 which is defined directly in terms of a traction-separation law. It is worth mentioning that
 458 cohesive behavior damage on the surface is an interaction property, not a material property
 459 [45]. Figure 15 shows that in the masonry portion describing the mesoscale model, the size

460 of the units has to be expanded by the mortar thickness h_m in both directions. A linear elastic
 461 traction separation behavior was assumed in the interaction model followed by the initiation
 462 and evolution of the damage. The nominal traction stress vector, $\{t\}$, was determined by three
 463 components: a normal stress value (t_n) in the perpendicular direction on the cohesive
 464 behavior surface, and two transverse shear stresses (t_s and t_t). The elastic behavior is given
 465 as,

$$t = \begin{Bmatrix} t_n \\ t_s \\ t_t \end{Bmatrix} = \begin{bmatrix} K_{nn} & K_{ns} & K_{nt} \\ K_{ns} & K_{ss} & K_{st} \\ K_{nt} & K_{st} & K_{tt} \end{bmatrix} \times \begin{Bmatrix} \varepsilon_n \\ \varepsilon_s \\ \varepsilon_t \end{Bmatrix} = K \times \varepsilon \quad (3)$$

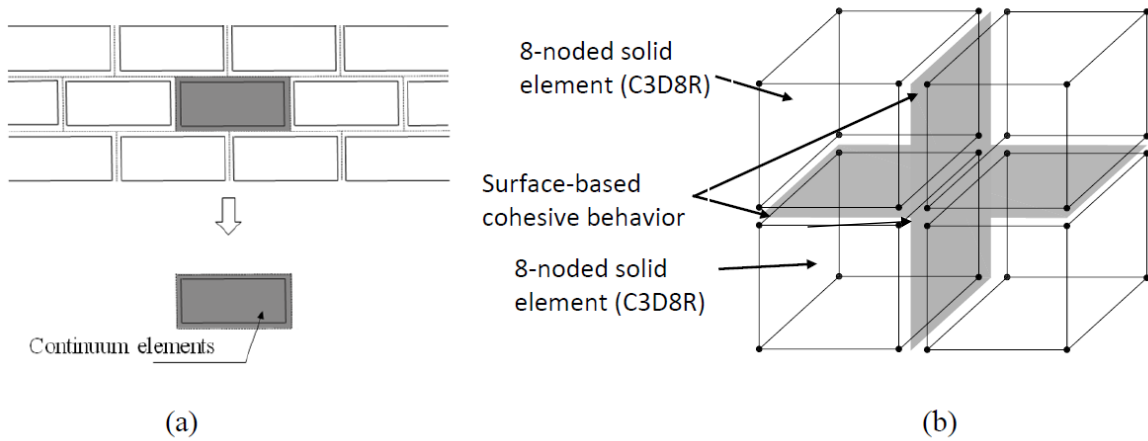
466 where K is the elastic stiffness matrix for fully coupled behavior. The stiffness matrix can be
 467 simplified to a diagonal matrix if the uncoupled behavior between the normal and shear
 468 behavior is considered. The normal and tangential stiffness coefficients are defined by
 469 Lourenço [46], which are given as:

$$K_{nn} = \frac{E_u E_m}{h_m (E_u - E_m)} \quad (4)$$

$$K_{ss} \text{ and } k_{tt} = \frac{G_u G_m}{h_m (G_u - G_m)} \quad (5)$$

470 where E_u and E_m are Young's moduli of the masonry units and mortar, G_u and G_m are their
 471 corresponding shear moduli, respectively. h_m is the actual thickness of the joints, the 10mm
 472 thick mortar joints are assumed for this purpose. The stiffness values obtained from the equations
 473 do not correspond to a penalty contact method, which means that the overlap of adjacent
 474 units becomes obvious under compression. This is a phenomenological description of
 475 masonry crushing because the failure process in compression is described by the
 476 microstructure of units and mortar and the interaction between them. In this study, the
 477 calculated values of K_{nn} , K_{ss} , and K_{tt} are 222 N/mm³, 99 N/mm³ and 99 N/mm³, respectively.
 478 When the damage initiation criterion is achieved based on the defined tractions between the
 479 masonry interface shear and tensile strength of the joints. The quadratic stress criterion is
 480 used to define damage initiation. This criterion is suitable when the quadratic stress ratios of
 481 masonry interfaces are equal to 1.0. The criterion was adopted as it effectively predicts the
 482 damage initiation of joints subjected to mixed-mode loadings [47], which is the case in
 483 masonry joint interfaces. The masonry joint interfaces are sub-subjected to tensile stress in
 484 the normal direction and shear stress in the two shear directions [48].

485



486

487

488

Figure 15 Models of masonry units and the interfaces (a) Masonry portion describing mesoscale model (b) masonry units and surface-based cohesive behavior

489

4.2 Validation of FEM model

490

491

492

493

494

495

496

497

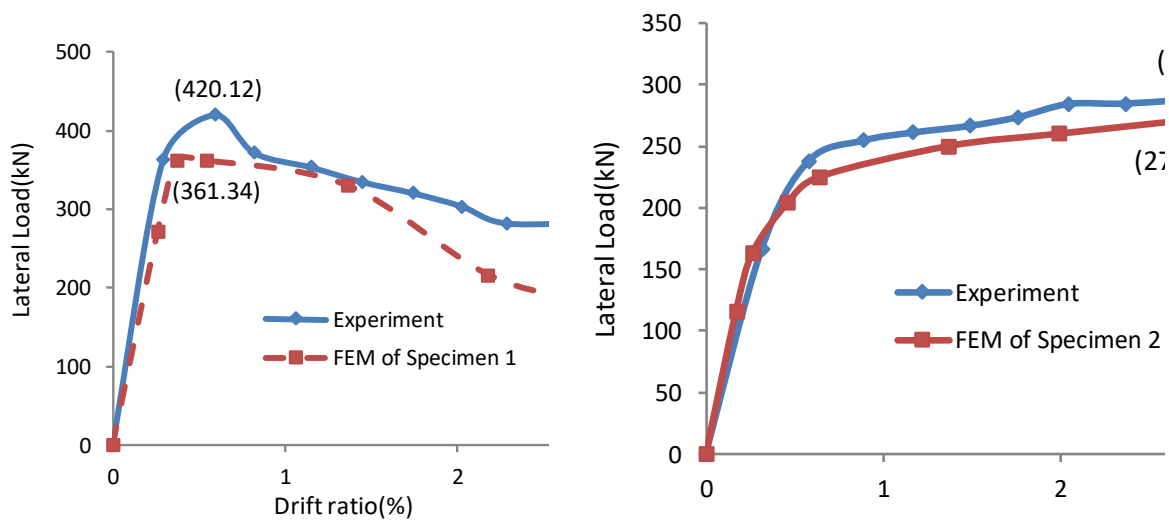
498

499

500

501

Figure 16 shows the comparison between the experimental curves (average values in both directions) and simulated load-displacement curves of the two control RC frame specimens. The results show that the FEM model evaluates the experimental behavior of the frames with a good agreement. The simulated results of the frame with sliding layers were 15% smaller than the experimental results after the elastic stage in both specimens. Therefore, the simulated load-displacement response of the frame was accepted, as shown in Figure 16. Table 4 lists the comparison details of the curves, including initial stiffness (K_{ini}) determined as the slope of the initial linear portion of the curves, as well as the ultimate load and ultimate displacement (P_{ult} and Δ_{ult}). The results show that the ultimate load and displacement of both frames are evaluated well with a maximum error ratio of 14% and 23%, respectively. The initial stiffness of the frame using the SBS layers was assessed well with an error ratio of 18%.



(a) Specimen 1

(b) Specimen 2

Figure 16 Comparison between experimental and simulated results

502

Table 4 Comparison between simulated and experimental results

503

Specimen	$K_{ini(FEM)}$ (kN/mm)	$K_{ini(EXP)}$ (kN/mm)	$K_{ini(FEM)}/$ $K_{ini(EXP)}$	$P_{ult(FEM)}$ (kN)	$P_{ult(EXP)}$ (kN)	$P_{ult(FEM)}/$ $P_{ult(EXP)}$	$\Delta_{ult(FEM)}$ (mm)	$\Delta_{ult(EXP)}$ (mm)	$\Delta_{ult(FEM)}/$ $\Delta_{ult(EXP)}$
1	32.31	38.45	1.19	361.34	420.12	0.86	45.15	36.76	1.23
2	19.26	16.39	1.18	271.76	290.14	0.94	88.61	95.58	0.93

504

5 Discussion on the test and FEM results

505

In this section, a parametric analysis using the FEM models developed above was conducted to study the failure modes and the effect of the sliding layers on the seismic behavior of the infilled frames. All analyses and discussions were based on FEM models and observed test results in the study. Table 5 shows the arrangement of the sliding layers inside the simulation specimens (Model I ~Model IX), in which Model II is Specimen 2 tested in the study as a control specimen.

512

Table 5 Details of simulation specimens in the parametric study

513

Layer materials	The number and spacing of sliding layers (L_s) in the filled walls		
	One layer ($L_s=1500mm$)	Two layers ($L_s=1000mm$)	Three layers ($L_s=750mm$)
SBS	Model I	Model II (Specimen 2)	Model III
Steel plate	Model IV	Model V	Model VI
BFRP laminate	Model VII	Model VIII	Model IX

514 **5.1 Failure modes**

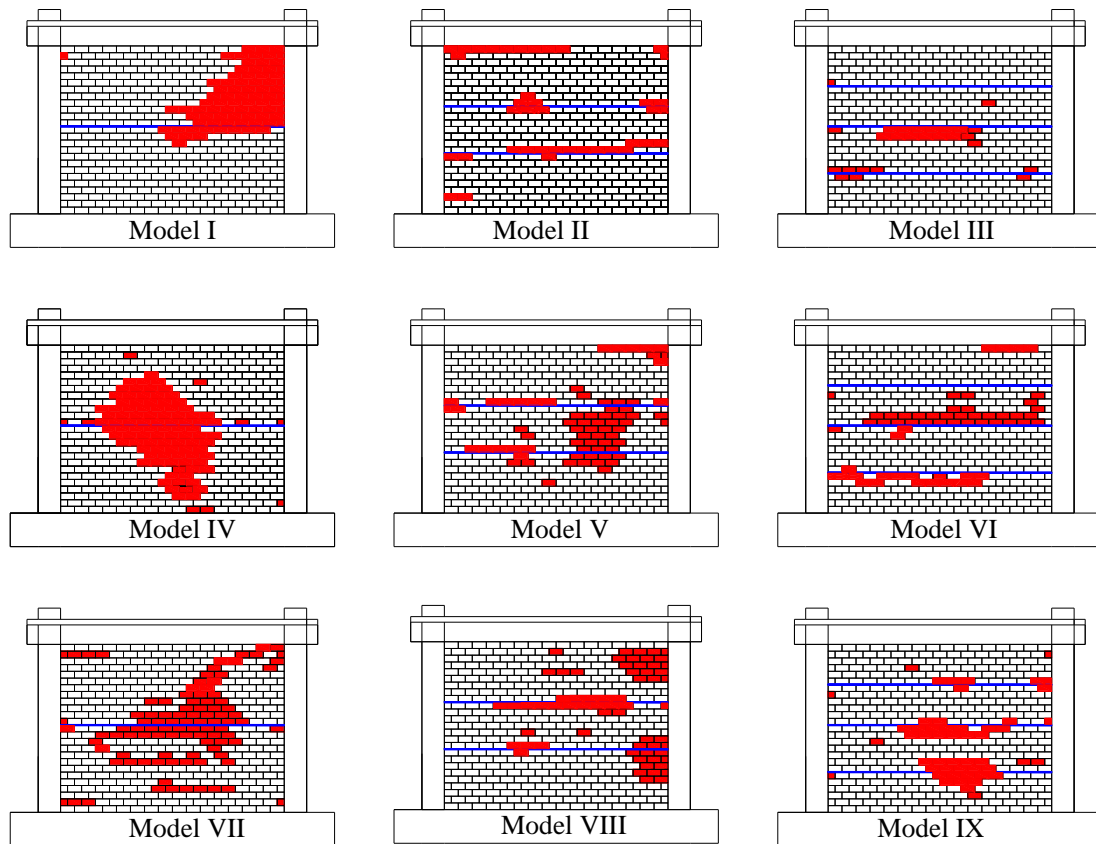
515 Figure 17 shows damaged areas for all tested and numerical specimens, while Table 6
 516 lists a summary of the main results including the maximum load and corresponding
 517 displacement, the initial stiffness, and the failure modes of the frames. The results show that
 518 the failure modes of the filled walls change from DC or CC mode to SS mode when the
 519 sliding layers are applied inside. This was also verified by the experimental results in the
 520 study and the literature [28]. Here, Specimen R1 (RC frame 0% in [28]) in previous research,
 521 a fully infilled frame without openings similar to Specimen 1, was applied here for a
 522 comparative study. The difference from Specimen 1 was that the connecting rebars were not
 523 full length and only had a length of 700mm. The failure mode of Specimen R1 was DC+CC
 524 mode, because (1) the length of connecting steel rebars was insufficient and (2) the strength
 525 of the filled wall was low. The masonry units in the central zone of the wall were first
 526 destroyed under reversed cyclic lateral loads. The damaged area increased and extended to
 527 the diagonal zones of the frame finally to form DC+CC failure mode. However, Specimen 2
 528 and other specimens used more than one sliding layer, the filled wall was divided into
 529 multiple parts by the layers which then weakened the diagonal strut effect in the whole
 530 infilled wall. This led to the frame being damaged with the SS failure mode. The results listed
 531 in Table 6 show that the main model of the frames with sliding layers is SS failure mode,
 532 especially when the number of layers increases. The DC mode and CC mode disappeared
 533 when the number of layers was large. Moreover, the smaller the friction coefficient of sliding
 534 layers was, the easier this effect changed.

535

536 **Table 6 A summary of the simulated results of the FEM specimens**

Specimens	Initial stiffness (kN/mm)	Ultimate loads (kN)	Ultimate displacements (mm)	Collapse ratio [28] (%)	Failure Modes
Model I	23.73	263.4	90.0	18.6	SS+CC
Model II	28.05	268.3	86.25	9.5	SS
Model III	15.45	242.3	69.88	6.38	SS
Model IV	28.80	365.9	89.70	24.88	SS+DC
Model V	29.14	331.1	71.4	17.13	SS+DC
Model VI	27.58	321.3	71.9	13.75	SS
Model VII	29.23	358.7	89.1	23.80	SS +DC
Model VIII	29.07	316.4	71.5	15.00	SS+CC
Model IX	30.86	333.4	89.2	12.03	SS

537



538

539

Figure 17 Damages and collapse of the simulated specimens (Model II= Specimen 2)

540

5.2 Effects of sliding layers

541

To understand the effect of sliding layers on the seismic behavior and damage of the masonry infilled frames under cyclic loads, such as load-displacement response and wall collapse ratio, comparative analysis based on the FEM simulation results was performed, including the effects of the spacing of the sliding layers and the materials of the layers.

544

545

(1) Effect of the spacing of the layers (L_s)

546

When a SBS layer is paved in the infills (Model I), the diagonal strut effect is interrupted at the sliding layer. When the number of sliding layers increases, the strut effect gradually disappears, and the damage to the infilled wall is concentrated at the sliding layer or the connection between the sliding layer and the column, indicating that SBS sliding layers weaken the strut effect resulting in a significant reduction in the in-plane damage of infilled wall. Figure 18 (a) shows a comparison of the load-displacement curves of the specimens with a different number of SBS layers. The specimens using one and two SBS layers presented a similar behavior until $R=1.5\%$, but the specimen with three layers possessed a much lower capacity than the others. From the point of view of reducing in-plane damage

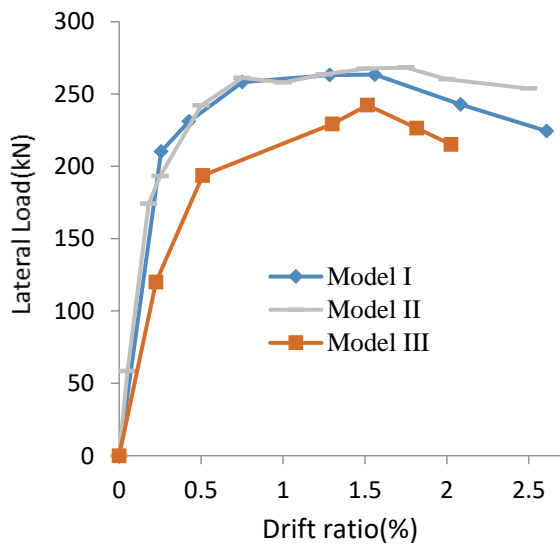
552

553

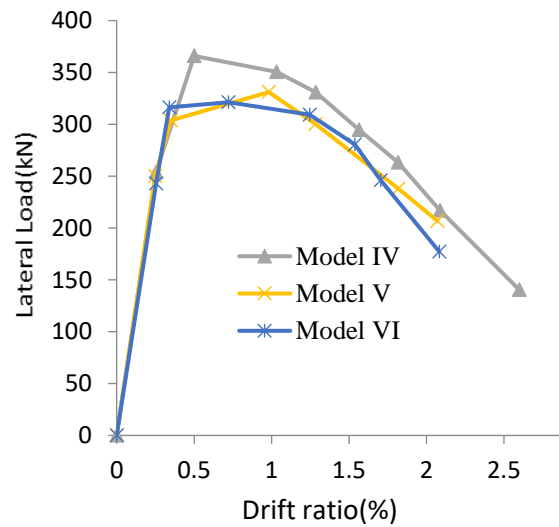
554

555 and improving in-plane bearing capacity for the infills, the preferred spacing of the SBS
 556 sliding layer in the infill wall is 1000mm.

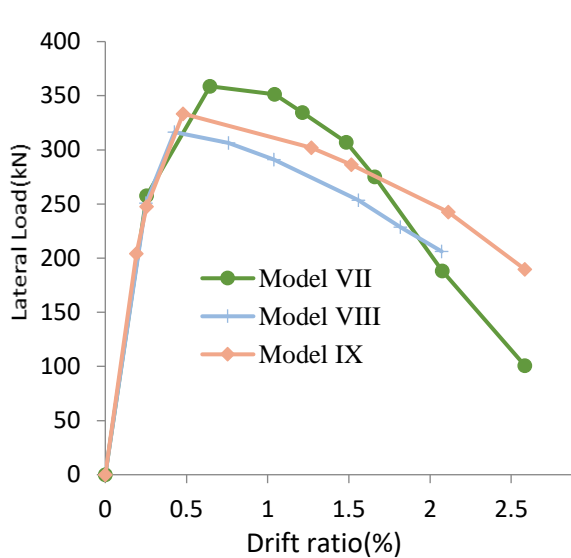
557 On the other hand, all specimens using steel plates possessed the same early linear
 558 behavior at the early stage until their ultimate loads, and then the lateral stiffness of the frames
 559 began to decrease. This is mainly due to the high coefficient of friction of the sliding layers.
 560 The increasing number of layers of steel plate did not lead to a decrease in the capacity of the
 561 frames, on the contrary, using more SBS layers can increase the slippage between the layers
 562 and wall, which then resulted in a degradation in the peak loads. Therefore, as shown in
 563 Figure 18 (b), the number of layers has a negative influence on the peak loads of the frames
 564 but made the frames present a similar post-peak behavior to the model specimens. A similar
 565 result was confirmed in the specimens with BFRP laminate (see Figure 18 (c)). Because the
 566 BFRP layers are non-ductility materials with a large slippage, the load-carrying capacity of
 567 the frames with BFRP laminate layers is reduced significantly. The stiffness of the frames
 568 significantly decreased after peak load, especially for the frames with fewer laminate layers.
 569 However, the stiffness of the BFRP specimens decreased with an increasing number of
 570 sliding layers, similar to the cases using steel plates, which also is similar to previous research
 571 [49] [50]. Figure 18 (d) presents the load-displacement behavior of all specimens, indicating
 572 that the load-carrying capacity of the frames with SBS layers is much smaller than that of the
 573 other frames.



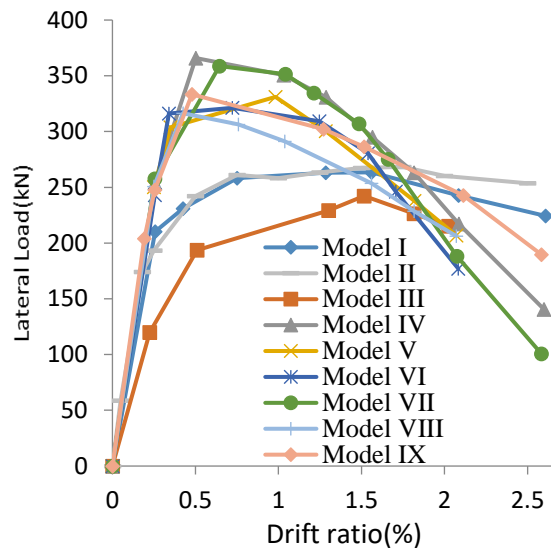
(a) Specimens with SBS layers



(b) Specimens with steel plates



(c) Specimens with BFRP laminates



(d) All specimens

574

Figure 18 Effect of the spacing of layers in the frames

575

(2) Effect of types of the materials of the layers

576

Figures 19 (a) to (c) show the load-displacement skeleton curves of the specimens with the same layer spacing but different sliding layer materials. When using the same layers of steel plate or BFRP laminate, the load-displacement behavior of the frames was the same, including initial elastic behavior, load-carrying capacity, and post-peak behavior. Due to the coefficient of friction of SBS layers, the use of the layers significantly reduced the ultimate load and accelerated the degradation of the load at post-peak. But the specimens using SBS layers can still present similar initial stiffness to the other specimens.

577

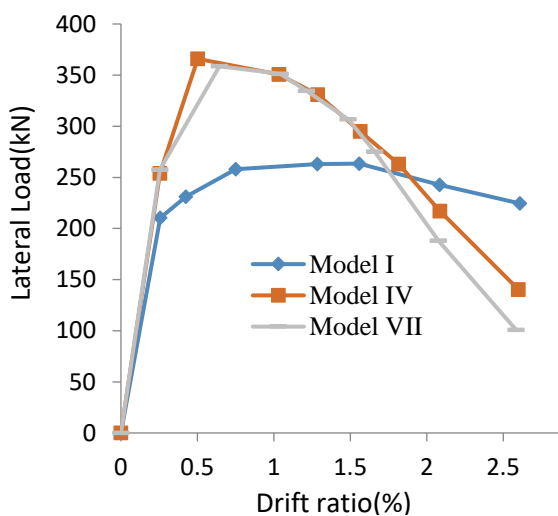
578

579

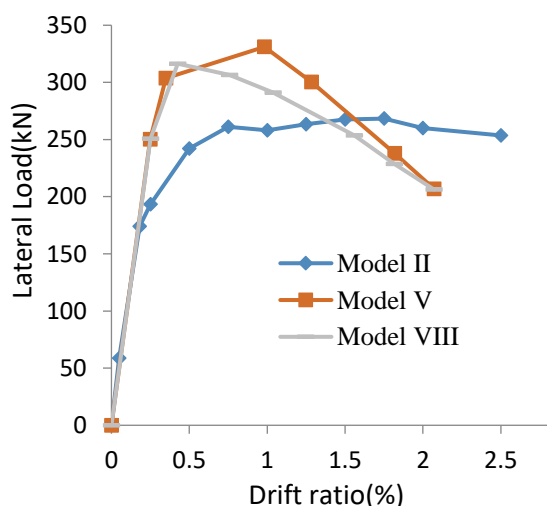
580

581

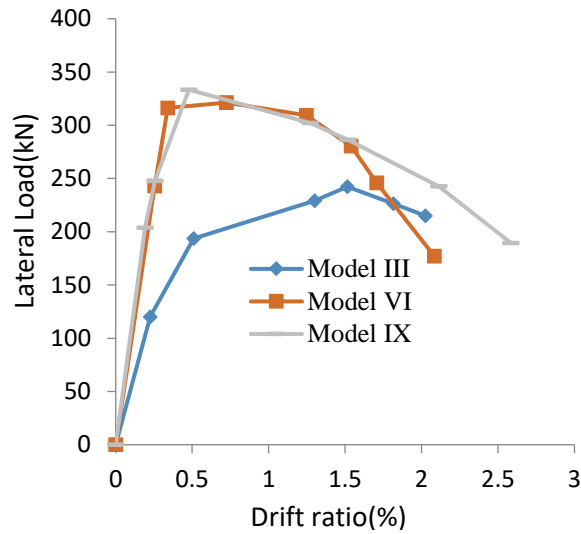
582



(a) $L_s=1500$ mm, one layer



(b) $L_s=1000$ mm, two layers



(c) $L_s=750$ mm, three layers

583 **Figure 19 Effect of the materials of sliding layers on infilled walls**

584 **5.3 Wall collapse ratios of infilled frames**

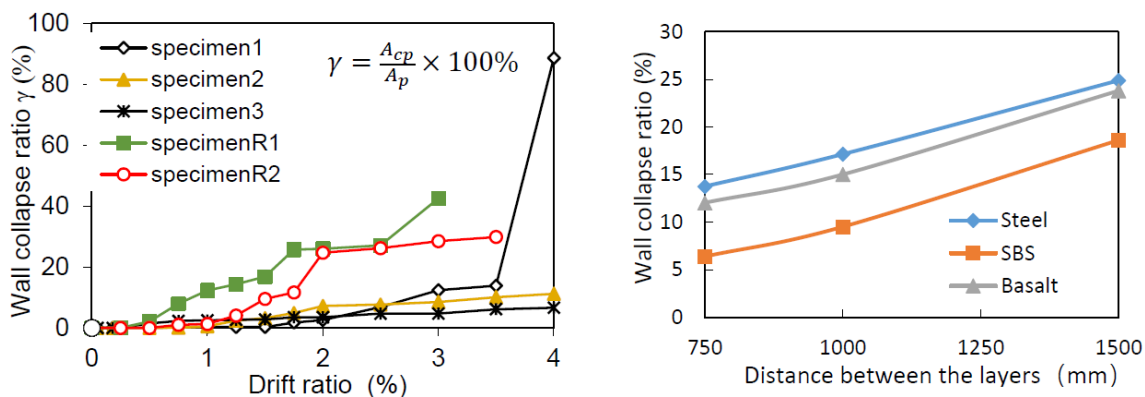
585 The wall collapse ratio γ proposed by the first and second authors [28] was used in
 586 this section to evaluate the damage evolution quantitatively of the infilled walls in RC frames,
 587 which is given as:

$$\gamma = \frac{A_{cp}}{A_p} \times 100\% \quad (6)$$

588 where A_{cp} is the collapsed and crushed area of infilled walls, A_p is the total area of the infilled
 589 wall of RC frames. To understand the influence of different measures on the in-plane damage
 590 of infilled walls, Specimen R1(RC frame 0% in [28]) and Specimen R2 (RC frame 25.7%
 591 in[28]) are applied here for a comparative analysis of the collapse of the MHB-infilled RC
 592 frames. The dimensions of frame elements and infilled materials in Specimens R1 and R2
 593 were the same as that of Specimen 1. The connecting rebar length of Specimens R1 and R2
 594 was only 700mm. Specimen R1 was a fully infilled frame (the opening ratio is 0%), and
 595 the opening ratio of Specimen R2 was 25.7%. The collapse ratio–drift ratio curves of the
 596 tested infills are shown in Figure 20 (a). Specimen 3 presented the lowest collapse ratio as
 597 drift ratios, $\gamma=6.63\%$, indicating it has the highest resistance to wall collapse in the frames.
 598 That can be attributed to two points: (1) the additional RC detailing columns improves the
 599 deformation capacity of the frame, and (2) the gaps relieved the compression of the wall in
 600 the corner from the frame columns on both sides. Specimen 1 showed the highest collapse
 601 ratio at $R=4\%$, which was 88.64%. The main damage occurred in the wall corners, and the
 602 bricks were also severely crushed. The diagonal strut significantly improved the load-
 603 carrying capacity at the early stage, but the collapse ratio of the wall was also the highest,
 604 and almost all the bricks and mortar were crushed in the state of cyclic compression shearing.
 605 Besides, specimen 2 presented a small collapse ratio of the wall, which was 11.2% at $R=4\%$,

606 in which the damage concentrated only in the sliding layers. The value was higher than that
 607 of the specimen with gaps but much smaller than that of the specimen with the fully infilled
 608 wall. This is due to the sliding layers improving the restoring of the RC frame compared to
 609 the fully infilled frame, but the improvement was slightly less than that of the frame with
 610 gaps. It can be found that the longer connecting rebars can reduce the damage to the infilled
 611 wall by comparing Specimen R1 and Specimen 1, and the openings are also helpful in
 612 reducing the damage to the infilled wall (Specimen R2), as shown in Figure 20(a).

613 On the other hand, as shown in Figure 20 (b), the collapse ratio of the infilled frames
 614 using SBS layers is much smaller than other specimens presenting similar wall collapse ratios.
 615 At the same time, the damaged area of the frames using more sliding layers was reduced
 616 significantly, regardless of the type of materials. The wall collapse ratios of the specimens
 617 decreased linearly with an increasing number of layers. Besides, it can be found that the
 618 longer connecting bars can reduce the damage to the infilled wall by comparing with the wall
 619 collapse ratio of Specimens R1 and 1 in Figure 20. It is also suggested that the openings are
 620 conducive to reducing the damage to infilled walls.



621 (a) Wall collapse ratio vs. drift ratio

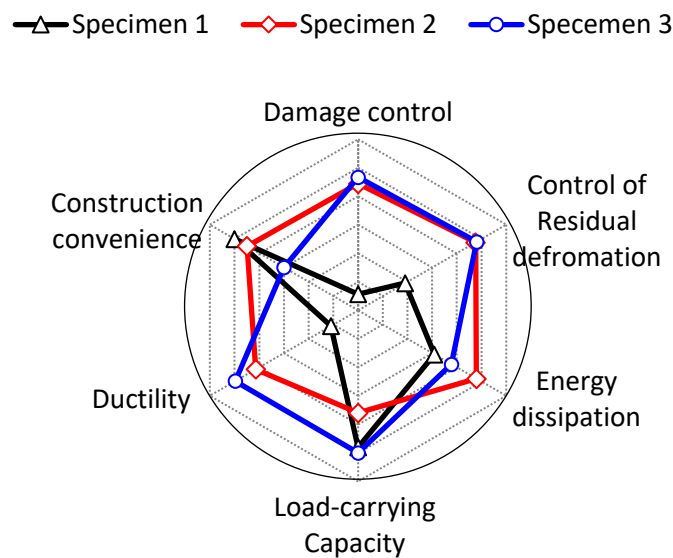
621 (b) Wall collapse ratio vs. layer spacing

622 **Figure 20 Wall collapse ratios of the infilled RC frames**

623 **5.4 Comparison of different control methods of infills in RC frames**

624 Based on the above experimental and numerical results described above, main
 625 discussions on different control methods in MHB-infilled RC frames were summarized here,
 626 including the load-carrying capacity, energy dissipation, residual drift ratio, damage ratio,
 627 construction convenience, and ductility of the specimens, as shown in Figure 21. For
 628 Specimen 1, the initial strong load-carrying capacity of the frame came from the strongest
 629 diagonal strut of the fully infilled wall. At the same time, fully infilling is also considered to
 630 be convenient for construction, compared to others. The main damages to the frame are the
 631 cracks in the frame and wall, wall collapse, brick compressive crushing, and the bending of
 632 connection rebars. However, the high residual deformation of the frame at the early stage
 633 hindered the resilience of the damaged infilled wall in the frame. The loss of the diagonal
 634 strut made the frame lower ductile than other frames due to sudden damage and collapse of

635 the infill wall. Since the determination of the maximum load carrying capacity of this type
 636 of structure was controversial in previous studies [29], it was proposed that the traditional
 637 ductility calculation methods were not suitable for MHB infilled frame structures. The
 638 observation results show that the deformation performance of this type of structure after the
 639 collapse of the wall was close to that of the bare frame structure. When the SBS layers were
 640 used, the residual deformation, damage control, and energy dissipation capacity of the infilled
 641 frame were improved significantly, but the construction convenience was not improved much
 642 and the capacity and ductility of the frame were slightly reduced. Except for the construction
 643 convenience and energy dissipation capacity, the use of gaps and detailing columns improved
 644 the other performance of the infilled frames, such as Specimen 3 in Figure 21.



645

646

Figure 21 Comparison of three control methods of the walls in the frames

647

6 Main conclusions

648

649

650

In this study, the seismic behavior of three one-bay one-story RC frames with masonry infilled walls with different damage control methods was experimentally and numerically investigated. The main conclusions are drawn here,

651

652

653

654

655

656

657

- (1). The walls of the fully infilled RC frame eventually collapsed, while the frame columns and beams were severely damaged locally. Its failure mode was diagonal crushing and the final failure of the wall of the frame was greatly controlled after adding sliding layers and using gaps with detailing columns. Among them, the main failure of the frame with sliding layers was the diagonal crushing between the layers, while that of the frame with gaps was the diagonal bracing crushing after the gaps are closed due to the damage and deformation of the frame.

- 658 (2). The fully infilled frame exhibited larger load-carrying capacity and stiffness
659 before wall collapse, and the highest energy dissipation capacity, but larger
660 residual deformation. After the infilled wall collapsed, the frame behaved as a
661 bare RC frame. The final residual deformation was relatively large due to the
662 accumulation of the damages in the early stage.
- 663 (3). Due to the addition of the SBS sliding layer, the stiffness of the infill walls was
664 reduced, resulting in the lateral stiffness and the peak load of the infilled frame
665 being reduced.
- 666 (4). The utilization of gaps and detailing columns allowed the load-carrying capacity
667 of the frame to be between the fully infilled frame and the frame with sliding
668 layers, before the gaps were closed, after which the frame exhibited as a fully
669 infilled frame. The frame presented an improved initial stiffness and energy
670 dissipation capacity compared with the frame with sliding layers.
- 671 (5). The parametric analysis results showed that the main failure of the frames using
672 sliding layers was SS failure mode, and the damage degree mainly depended on
673 the number of sliding layers. With more sliding layers, the damage of the frames
674 was better controlled, but their load-carrying capacity and energy dissipation were
675 reduced. Regarding the effect of the material type of sliding layers, steel plate and
676 SBS layers both exhibited similar damage control effectiveness. Based on the
677 study, using SBS sliding layers with a spacing of 1000 mm was recommended to
678 control the wall damage of the MHB-infilled frames.

679

680 **Acknowledgments**

681 The authors thank the support from the science and technology fund of Chengdu
682 fourth construction engineering of CDCEG, CCCC tunnel engineering company
683 limited (2021 R110121H01083).

684 **Declaration of Competing Interest**

685 The authors declare that they have no known competing financial interests or
686 personal relationships that could have appeared to influence the work reported in
687 this paper.

688 **Notations**

689 A_{cp} : collapsed and crushed area of infilled walls.

690 A_p : total area of the infilled wall of RC frames.

691 b : width of section.

692 b_f : width of flange

693 F : lateral load.

694 h : total thickness of section

695 h_f : total thickness of the flange
 696 K : unloading stiffness.
 697 K_{int} : initial stiffness.
 698 K_y : yielding stiffness.
 699 R_{res} : lateral residual deformation.
 700 V_{max} : maximum lateral load.
 701 W : maximum strain energy of a given cycle.
 702 CC: corner crushing mode.
 703 SS: sliding shear mode.
 704 DC: diagonal compression mode
 705 DK: diagonal cracking mode.
 706 FF: frame failure mode.
 707 Δ_y : yielding displacement.
 708 Δ_{max} : maximum displacement.
 709 Δ_u : ultimate displacement.
 710 μ_{max} : maximum ductility.
 711 μ_u : ultimate ductility.
 712 δ : lateral deformation
 713 δ_u : inter-story drift ratio
 714 δ_R : residual deformation.
 715 ν_{eq} : fraction of critical damping.
 716 ΔW : energy loss per cycle in sinusoidal vibration.
 717 γ : wall collapse ratio.

References

1. G. Uva, D. Raffaele, F. Porco, A. Fiore(2012). On the role of equivalent strut models in the seismic assessment of infilled RC buildings. *Engineering Structures*, 42, 83-94.
2. Bartolomeo Pantò, Ivo Caliò, Paulo B. Lourenço(2017). Seismic safety evaluation of reinforced concrete masonry infilled frames using macro modelling approach. *Bulletin of Earthquake Engineering*, 15(9), 3871-3895.
3. J. M. Proença, A. S. Gago, A. V Costa(2012) Strengthening of masonry wall load bearing structures with reinforced plastering mortar solution. *Proceedings of the 15th world conference on earthquake engineering*. No.2004,1-10.
4. A. Costa, J. Miranda Guedes, H. Varum(2014) *Structural Rehabilitation of Old Buildings*. Springer, Berlin, Heidelberg.
5. A. M. N. Goncalves, L. M. C. Guerreiro, P. Candeias, J. G. Ferreira, A. Campos Costa(2018)Characterization of reinforced Timber Masonry Walls in ‘Pombalino’ buildings with dynamic tests. *Engineering Structures*, 166, 93–106.
6. R. Soti, A. R. Barbosa, and A. Stavridis(2014)Numerical modeling of URM infill walls retrofitted with embedded reinforcing steel. *10th U.S. National Conference on Earthquake Engineering: Frontiers of Earthquake Engineering*, Anchorage, Alaska.
7. A. Triwiyono, A. S. B. Nugroho, A. D. Firstyadi, and F. Ottama(2015)Flexural strength and ductility of concrete brick masonry wall strengthened using steel reinforcement. *Procedia Eng.*, 12, 940–947.
8. Zhou Yun, Guo Yangzhao, Liao Yifa, et al(2013) Experimental study on the performances of damped infill

- wall unit. *China Civil Engineering Journal*, 46(5),56-63 (in Chinese).
9. F.C.Wang, T.B.Kang, Y.S.Yang, S.Lu.(2015)Seismic behaviour of the wall-frame structure infilled with rubber concrete brick. *Journal of Shengyang Jianzhu University*, 31(4), 661–670(in Chinese).
 10. Ye. Yanhua, Li Liquan, Sun Weimin, et al(2004) Experimental study on seismic behaviors of hollow block wall filled with foaming concrete. *Earthquake Engineering and Engineering Vibration*, 24(5),154-158 (in Chinese).
 11. Moghadam H A, Mohammadi M Gh, Ghaemian M(2006) Experimental and analytical investigation into crack strength determination of infilled steel frames. *Constructional Steel Research*, 12(62),1341-1352.
 12. Sahota M K, Riddington J R(2001) Experimental investigation into using Lead to reduce vertical load transfer in infilled frames. *Engineering Structures*, 23(1),94-101.
 13. Mohammad Aliaari, Memari A M(2005) Analysis of masonry infilled steel frames with seismic isolator subframes. *Engineering Structures*, 27(4),487-500.
 14. Yang Wei, Ou Jinping(2011)A method of improving global seismic capacity based on failure-controlled of infill walls for infilled structures. *Building Structures*, 41(8),34-39 (in Chinese).
 15. Zhou Yun, Guo Yangzhao, Liao Yifa, et al(2014)Experimental study on seismic behavior of damped masonry in-filled reinforced concrete frame structures with SBS layers. *China Civil Engineering Journal*, 47(9),21-28 (in Chinese).
 16. R. Perera, S. Gómez, and E. Alarcón(2004) Experimental and Analytical Study of Masonry Infill Reinforced Concrete Frames Retrofitted with Steel Braces. *Journal of Structural Engineering*, 130(32) ,2032–2039.
 17. T. Sevil, M. Baran, T. Bilir, and E. Canbay(2011) Use of steel fiber reinforced mortar for seismic strengthening. *Construction and Building Materials*, 25(2),892–899.
 18. T. S. Yaman, E. Canbay(2014)Seismic strengthening of masonry infilled reinforced concrete frames with steel- fibre-reinforced mortar. *ICE Proceedings Structures and Buildings*,167(1), 3-14.
 19. G. Erol , H. F. Karadogan(2016) Seismic strengthening of infilled reinforced concrete frames by CFRP. *Composite. Part B: Engineering*, 91, 473–491.
 20. J. B. Mander, L. E. Aycardi, D. K. Kim(1994) Physical and Analytical Modeling of Brick Infilled Steel Frames. *Technical Report*, NCEER 94-0004, Buffalo.
 21. A. A. Hamid, W. W. El-dakhkhni, M. Asce, Z. H. R. Hakam, M. Elgaaly, F. Asce(2005)Behavior of Composite Unreinforced Masonry – Fiber-Reinforced Polymer Wall Assemblages Under In-Plane Loading. *Journal of Composites for Construction*, 9(1), 73–83.
 22. T. C. Triantafillou(1998) Shear Strengthening Of Reinforced Concrete Beams Using Epoxy-Bonded FRP Composites. *ACI Structural Journal*, 95(2),107-115.
 23. M. Preti, N. Bettini, L. Migliorati, V. Bolis, A. Stavridis, G. A. Plizzari(2016)Analysis of the in-plane response of earthen masonry infill panels partitioned by sliding joints. *Earthquake Engineering & Structural Dynamics*, 45(8) ,1209–1232.
 24. M. Preti, M. Neffati, V. Bolis(2018)Earthen masonry infill walls: Use of wooden boards as sliding joints for seismic resistance. *Construction and Building Materials*, 184, 100–110.
 25. M. Preti, V. Bolis, A. Stavridis(2019)Seismic infill–frame interaction of masonry walls partitioned with horizontal sliding joints: analysis and simplified modeling. *Journal of Earthquake Engineering*, 23(10) , 1651-1677.
 26. Ivo Calìò, Bartolomeo Pantò(2014)A macro-element modelling approach of Infilled Frame Structures. *Computers and Structures*, 143,91-107.
 27. Prateek Kumar Dhir, Enrico Tubaldi,Hamid Ahmadi, et al(2021)Numerical modelling of reinforced concrete frames with masonry infills and rubber joints. *Engineering Structures*, 246,112833.
 28. Su. Q. W., Cai G. C., Cai H. R. (2017) Seismic behaviour of full-scale hollow bricks-infilled RC frames under cyclic loads. *Bulletin of Earthquake Engineering*, 15(7), 2981-3012.
 29. Cai, G.C., Su, Q.W. (2019) Effect of infills on seismic performance of reinforced concrete frame structures—A full-scale experimental study. *Journal of Earthquake Engineering*, 23(9), 1531-1559.
 30. Ministry of Housing and urban-Rural Development of the PRC(2002) Standard for test method of mechanical properties on ordinary concrete (GB/T 50081-2002). Beijing, China Building industry press.

31. Ministry of Housing and urban-Rural Development of the PRC(2010) Code for design of concrete structures (GB50010-2010). Beijing, Standards press of China.
32. State General Administration of the People's Republic of China for Quality Supervision and Inspection and Quarantine(2018) Steel for the reinforcement of concrete—Part 2: Hot rolled ribbed bars(GB/T 1499.2-2018). Beijing, Standards press of China.
33. Ministry of Housing and urban-Rural Development of the PRC(2009) standard for test method of performance on building mortar(JGJ/T70-2009).Beijing, China Building industry press.
34. T. Paulay , M. N. Priestley(1992) Seismic design of reinforced concrete and masonry buildings, John Wiley & Sons, Inc.
35. H. Pam, A. Kwan, M. S. Islam(2001)Flexural strength and ductility of reinforced normal-and high-strength concrete beams. *Proceedings Of The Institution Of Civil Engineers: Structures And Buildings*,146(4),381-389.
36. Jacobsen LS (1960) Damping in composite structures. In: Proceedings of the 2nd world conference on earthquake engineering, 2, 1029–1044.
37. W. W. El-dakhkhni, S. M. Asce, M. Elgaaly, F. Asce, A. A. Hamid(2003)Three-Strut Model for Concrete Masonry-Infilled Steel Frames, *Journal of Structural Engineering*, 129(2),177-185.
38. C. E.-I. Du Beton(1996) RC frames under earthquake loading: state of the art report. T. Telford, London.
39. D. J. Carreira , K.H. Chu(1985)Stress-strain relationship for plain concrete in compression. *Journal of the American Concrete Institute*, 82(6),797-804
40. D. J. Carreira and K.H. Chu(1986)Stress-strain relationship for reinforced concrete in tension. *Journal of the American Concrete Institute*, 83(1), 121–28.
41. J. Lubliner, J. Oliver, S. Oller, E. Onate(1989) A plastic-damage model for concrete. *International Journal of Solids and Structures*, 25(3), 299–329.
42. J. Lee , G. L. Fenves(1998) Plastic-damage model for cyclic loading of concrete structures.*Journal of Engineering Mechanics*,124(8), 892–900.
43. Abaqus GUI. Abaqus 6.11. Users Manual 6.11, 2011.
44. K. J. William, E. . P. Warnke(1974)Constitutive model for the triaxial behavior of concrete. *Proceedings of the International Association for Bridge and Structural engineering*, 1–30.
45. Wang Y. Y.(2020) Abaqus analysis user's guide : element.China Mechine Press, Beijing(in Chinese).
46. P. B. Lourenço(1996). Computational strategies for masonry structures, Ph.D. Thesis, 1996. Available from: <www.civil.uminho.pt/masonry>.
47. Campilho RD. De Moura M, Domingues J(2008)Using a cohesive damage model to predict the tensile behaviolur of CFRP single-straprepairs. *International Journal of Solids and Structures*, 45 (5):497-512.
48. Kurdo F. Abdulla, Lee S. Cunningham, Martin Gillie(2017)Simulating masonry wall behaviour using a simplified micro-model approach. *Engineering Structures*,151:349-365.
49. B. A. Mehrabi, P. B. Shing, P. S. Michael, L. N. James(1996) Experimental Evaluation of Masonry-Infilled RC Frames. *Journal of Structural Engineering*, 122(3), 228–237.
50. Al-Chaar G. K. (1998) (1998)Non-Ductile Behavior of Reinforced Concrete Frames With Masonry Infill Panels Subjected to In-Plane Loading, Chicago , the University of Illinois at Chicago.